POLITECNICO
MILANO 1863

RE.PUBLIC@POLIMI
Research Publications at Politecnico di Milano

Post-Print

This is the accepted version of:

A. De Vittori, Z. Pavanello, P. Di Lizia, J. McMahon, R. Armellin
Combined Long-Term Collision Avoidance and Stochastic Station-Keeping in Geostationary Earth Orbit
Journal of Guidance Control and Dynamics, Vol. 48, N. 4, p. 840-854, 2025 (published online 20/02/2025)
doi:10.2514/1.g008629

The final publication is available at https://doi.org/10.2514/1.g008629

Access to the published version may require subscription.

When citing this work, cite the original published paper.

Permanent link to this version
http://hdl.handle.net/11311/1284817

Combined Long-Term Collision Avoidance and Stochastic Station-Keeping in GEO

Andrea De Vittori *
Department of Aerospace Science and Technology, Politecnico di Milano, Milan, MI, 20156, Italy.

Zeno Pavanello †
Te Pūnaha Ātea - The Space Institue, The University of Auckland, Auckland 1010, New Zealand.

Pierluigi Di Lizia ‡
Department of Aerospace Science and Technology, Politecnico di Milano, Milan, MI, 20156, Italy.

Jay McMahon §
University of Colorado Boulder, Ann and H.J. Smead Aerospace Engineering Sciences, 3775 Discovery Dr, Boulder 80303, Colorado, United States.

Roberto Armellin ¶
Te Pūnaha Ātea - The Space Institue, The University of Auckland, Auckland 1010, New Zealand.

To limit the spread of space debris, Space Situational Awareness (SSA) delineates guidelines to preserve current space assets. Developing effective Collision Avoidance Maneuver (CAM) strategies is emerging as a global top priority among the considered countermeasures to debris-generating events. Despite most encounters happening over very short time frames, some conjunctions occur over a longer time window, such as in Geostationary Earth Orbit (GEO), where the involved objects may have small relative velocities. Besides, external perturbations, particularly the geopotential, lunisolar, and Solar Radiation Pressure (SRP) ones, exert forces on the spacecraft, causing it to deviate from its designated slot and potentially endanger neighboring satellites. This issue is compounded when considering state uncertainty. The presented work, therefore, introduces convex optimization approaches for long-term CAM and tailored stochastic Station Keeping (SK) policy regarding longitude and latitude in this regime. The formulation enables continuous CAM and Chance Constrained Station-Keeping (CCSK), ensuring satellite adherence to an assigned GEO slot with a given probability. Two kinds of chance constraints are devised: the first one does not consider the correlation between longitude

*Post Doctoral Researcher, Department of Aerospace Science and Technology, Politecnico di Milano, via Privata Giuseppe La Masa 34, 20156. Email: andrea.devittori@polimi.it.

†PhD student, Te Pūnaha Ātea - Space Institute, 20 Symonds Street, Auckland Central, Auckland 1010, New Zealand. Email: zpav176@aucklanduni.ac.nz.

‡Associate professor, Department of Aerospace Science and Technology, Politecnico di Milano, via Privata Giuseppe La Masa 34, 20156. Email: pierluigi.dilizia@polimi.it.

§Associate Professor, University of Colorado Boulder, Ann and H.J. Smead Aerospace Engineering Sciences, 3775 Discovery Dr, Boulder 80303, Colorado, United States. Email: jay.mcmahon@colorado.edu.

¶Professor, Te Pūnaha Ātea - Space Institute, 20 Symonds Street, Auckland Central, Auckland 1010, New Zealand. Email: roberto.armellin@auckland.ac.nz.

and latitude, but the latter does.

I. Introduction

Throughout the space age, a multitude of satellites have been launched, leading to the monitoring of over 23,000 objects within the Near Earth environment, encompassing both operational and defunct satellites. The vast majority of orbiting clutter consists of minuscule fragments challenging to detect using current technologies and high-speed debris scattered across various areas of interest [1]. Among these, Low Earth Orbit (LEO) and Geostationary Earth Orbit (GEO) stand as the most densely populated realms, with GEO being particularly critical for communication, observation, and weather forecasting purposes. GEO is primarily populated by upper stages, apogee boost motors, and mission-related equipment, alongside non-functional satellites that, upon reaching the end of their operational lifespan, jeopardize other active satellites [2]. In this region, a spacecraft is subject to geopotential, lunisolar, and Solar Radiation Pressure (SRP) disturbances: it may veer off course from its predefined Station Keeping (SK) box, demarcated by specific longitude and latitude coordinates. To prevent potential collisions with neighboring satellites, operators frequently conduct SK cycles [3] to ensure the spacecraft remains within its designated zone. When a close approach with a Resident Space Object (RSO) is flagged as risky, ground controllers optimize a Collision Avoidance Maneuver (CAM) by either anticipating or postponing SK operations. The risk of a collision is quantified using a stochastic variable, the Probability of Collision (PoC). According to V. Coppola in [4], PoC is the likelihood that the separation distance between two celestial objects will decrease to a value below a specified threshold within a time frame of interest.

In general, conjunction events are deemed too hazardous when PoC surpasses specific thresholds. Yellow and red warnings corresponding to PoC limit values of 10^{-5} and 10^{-4} respectively, have been defined by NASA [5]. In such instances, CAMs are designed to lower PoC while adhering to operational constraints. The CAM strategy must be tailored to address the specific nature of the encounter. Indeed, in the state of the art, conjunctions are categorized into two broad categories, short-term and long-term, as represented in Fig. 1. Short-term events, quite common in LEO, involve two objects with a high relative velocity. This makes the conjunction almost instantaneous, and it allows for the representation of the dynamics in the encounter's B-plane and for a simplified calculation of PoC [6]. Conversely, in long-term conjunctions, which are more likely to happen in GEO [2], the objects move on similar orbits with a low relative velocity, and the encounter cannot be considered instantaneous. Patera [7] demonstrates that if the relative trajectory of the satellite with respect to the RSO deviates significantly from a straight line within the combined covariance ellipsoid, the encounter is deemed long-term. In this case, it becomes necessary to resort to more complex ways of computing PoC because the dynamics cannot be represented in the B-plane [4, 7]. For short-term PoC models, long-term ones are much more computationally demanding, and they involve the use of a larger number of nonlinear operations [8–11]. For this reason, rigorous CAM design to lower PoC in such scenarios is rather complex. Nonetheless,

recent research [12, 13] suggests using the Instantaneous Probability of Collision (IPoC) as a proxy for PoC. In a long-term encounter scenario, IPoC is much easier and faster to compute than PoC [14]. Thus, it is acceptable to design the CAM by controlling IPoC, which indirectly regulates the PoC growth [15, 16].

Strategies for CAMs during long-term encounters have been proposed in the literature, utilizing Linear Programming (LP) [17], deterministic disjunctive LP [18], and convex optimization [15] methods. In the approach outlined by Mueller in reference [17], the relative motion is simplified through a linear time-varying system, transforming the Collision Avoidance (CA) problem into a LP. This process involves linearizing the ellipsoidal Keep-Out-Zone (KOZ) constraint into a hemispace. Additionally, to maintain linearity in the problem, the minimization of the l^1 norm of the control is employed, potentially leading to increased propellant consumption compared to using the l^2 norm. It's worth noting that Mueller's method does not account for state uncertainties; instead, the author arbitrarily defines the KOZ region. Serra et al. [18] introduce a deterministic disjunctive LP approach, wherein the dynamics are linearized using the Yamanaka-Ankersen State Transition Matrix (STM), which also facilitates linear covariance propagation. Similar to our approach, Serra et al. substitute PoC with IPoC, although this variable is not directly controlled. Instead, a polyhedral KOZ constraint is implemented, and IPoC is only assessed post-validation. Furthermore, as in [17], their approach leans on the same l^1 norm of the control history. This work draws inspiration from the framework set by Pavanello et al. [19] for computing fuel-optimal CAMs during long-term encounters. The CAM problem is solved as a Sequential Convex Programming (SCP), utilizing successive convexification of dynamics and a projection and linearization algorithm for the KOZ constraint, ensuring the constraint is respected continuously over the long-term encounter period. Deterministic SK constraints are used to combine the CAM with the SK maneuver. Moreover, the solution's robustness is enhanced by introducing a sensitivity condition for the collision metric with a trust region definition to mitigate linearization effects [20–22]. With respect to the previous methods, the use of a succession of Second Order Cone Programs (SOCPs) allows for the definition of second-order cone constraints, which grant the minimization of the l^2 norm of the control history, thus ensuring fuel-optimal solutions. Convex optimization is chosen due to its proven efficacy in solving complex problems in aerospace engineering [23], being successfully employed in a spectrum of trajectory design scenarios [24], spanning from short-term CAMs [25–29] to tasks such as spacecraft formation reconfiguration [30], powered descent, and landing [31, 32].

Expanding on the research presented in [15], this work aims to augment the combination of CAM and SK maneuvers by developing a stochastic SK constraint. The use of chance constraints embeds into the optimization problem the probability of residing inside a SK box. Stochastic optimization with chance constraints involves optimizing decision variables under uncertainty, ensuring they are satisfied with a specified probability level. It balances the trade-off between optimizing objectives and managing the risk associated with uncertain parameters. The literature contains numerous applications of this optimization technique. R. Chai et al., in [33], explore a computational framework rooted in optimal control to address stochastic trajectory optimization with the integration of chance constraints. They

adopt a time discretization to parameterize uncertain variables, forming the trajectory ensemble. Subsequently, the resulting problem is tackled with conventional optimal control solvers. To ensure dependable gradient information for the optimization algorithm, a smooth and differentiable chance-constraint approximation method is introduced, replacing the original probability constraints. Stochastic optimization [34] has also been included in the optimal flight of aero-assisted reentry vehicles during the atmospheric entry flight phase while taking into account both deterministic and control chance constraints. B. Benedikter et al. introduce a method for designing optimal space trajectories under significant uncertainty driven by finite-horizon covariance control in [35]. This technique plans an optimal path and a robust feedback controller to manage in-flight disturbances. It converts the nonlinear problem into a deterministic convex optimization one, achieved by changing variables to relax constraints. J. K. Knaup et al., in [36], explore the finite-horizon optimal covariance steering problem for discrete-time linear systems subject to both additive and multiplicative uncertainties as well as state and input chance constraints. In particular, a tractable convex approximation of the optimal covariance steering problem is developed by tightening the chance constraints and introducing a suitable change of variables. S. Boone et al., as referenced in [37], [38], and [39], demonstrate methods for maintaining spacecraft within a predefined domain given a specified probability across different orbits and dynamics. They employ State Transition Tensors (STTs) to accommodate the nonlinear evolution of state uncertainties and simplify the boundary constraints.

This work combines CAM and stochastic SK in an all-in-one maneuver over a long-term encounter. The spacecraft is initially confined within a slot with precise longitude and latitude limits. As uncertainty grows, these boundaries evolve, traditionally defined through a disjoint chance-constraint formulation, which is not conservative with highly correlated stochastic variables.

We present a refined approach that integrates 2D joint constraints for rectangular keep-in domains, effectively accounting for correlation. This method is adaptable to higher dimensions and can be easily embedded in any Successive Convexification (SCvx) problem requiring a joint chance-constrained formulation.

The first part of the paper, in Sec. II, revolves around the theoretical foundation of chance constraints implementation in trajectory design problems. Sec. III provides a general view of the integrated CAM and SK, addressing not only the standard chance constraint formulation but also how to face joint constraints. The paper continues with the results in Sec. IV showing important figures of merits and food for thought in Sec. V.

II. Fundamentals

A. Stochastic Chance Constraint Optimization

In decision-making under uncertainty, chance constraints offer a key methodology for managing risks. Unlike the deterministic counterparts, chance constraints incorporate probability to quantify the likelihood of violating specific

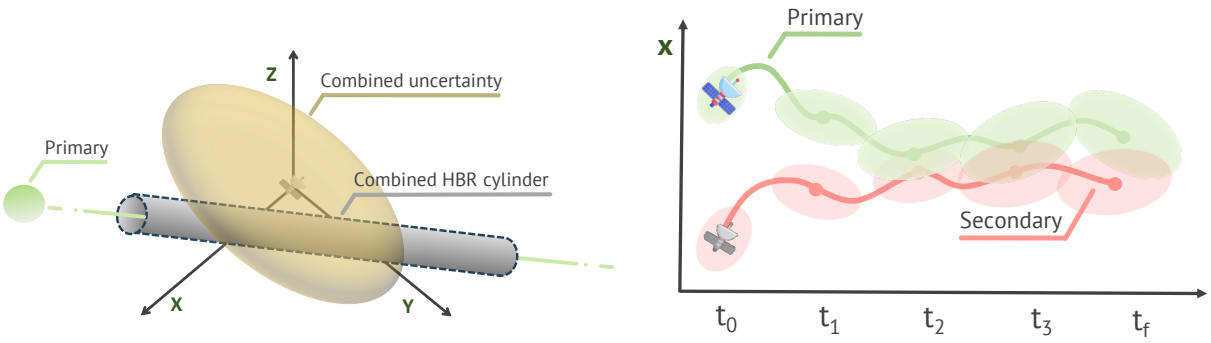

(a) **(b)**

Fig. 1 Short-term encounter in (a) a long-term one in (b).

conditions, expressed as inequalities. This mathematical framework is applied in stochastic trajectory optimization to restrain the spacecraft within a specific region in space.

Let us now assume that the controlled variables $\boldsymbol{x}(\xi) \in \mathbb{R}^{n_x}$ are subject to bounds that can be modeled as linear inequalities [40]:

$$\mathrm{P} = \left\{ \xi \in \Omega,\ \boldsymbol{h}^l \in \mathbb{R}^{n_x} \middle|\ \left(\boldsymbol{h}^l\right)^\top \boldsymbol{x}(\xi) \leq g^l, \quad l = 1, \ldots, N_\mathrm{c} \right\} \tag{1}$$

N_c is the overall number of scalar constraints. More concretely, the output $\boldsymbol{x}(\xi)$ should be contained in the polytope defined by N_c linear inequality constraints with probability larger than some arbitrary level α. Two typical chance constraint formulations are:

1) Individual chance constraints must be met separately with a user-specified level of certainty α^l with $\boldsymbol{\alpha} = [\alpha^1, \alpha^2, \ldots, \alpha^{N_\mathrm{c}}]^\top$ being a vector in $\mathbb{R}^{N_\mathrm{c}}$:

$$\Pr\left\{ \xi \in \Omega,\ \boldsymbol{h}^l \in \mathbb{R}^{n_x} |\ \left(\boldsymbol{h}^l\right)^\top \boldsymbol{x}(\xi) \leq g^l \right\} \geq \alpha^l, \quad l = 1, \ldots, N_\mathrm{c} \tag{2}$$

2) Joint chance constraints have to be met simultaneously with a prescribed level of certainty α:

$$\Pr\left\{ \xi \in \Omega,\ \boldsymbol{h}^l \in \mathbb{R}^{n_x} |\ \left(\boldsymbol{h}^l\right)^\top \boldsymbol{x}(\xi) \leq g^l, \quad l = 1, \ldots, N_\mathrm{c} \right\} \geq \alpha, \tag{3}$$

Usually, $\boldsymbol{\alpha}$ and α are reframed as a function of the violation probability:

$$\boldsymbol{\alpha} = \mathbf{1} - \boldsymbol{\delta}, \quad \alpha = 1 - \delta \tag{4}$$

Where $\boldsymbol{\delta} \in \mathbb{R}^{N_\mathrm{c}}_{(0,0.5]}$ and $\delta \in \mathbb{R}_{(0,0.5]}$. For context, the violation probability is greater than 0 because, assuming a Gaussian Probability Density Function (PDF) for $\boldsymbol{x}$, if the violation probability were 0, every realization would have to

be infinitely far from g^l. By contrast, a violation probability of 0.5 indicates that the constraint is satisfied if at least half of the PDF's realizations meet the inequality condition.

Handling individual chance constraints is straightforward due to the scalar nature of the probability density function under consideration. Enforcing such a bound is equivalent to adding a second-order cone constraint on the optimization problem. Individual chance constraints are constraints of the type:

$$\Pr\left\{\left(\boldsymbol{h}^l\right)^\top \boldsymbol{x}(\xi) \leq g^l\right\} \geq 1-\delta^l \tag{5}$$

which means that the probability that the random variable $\boldsymbol{x}(\xi)$ takes its value in the negative half-space is larger than $1-\delta^l$. Let $\boldsymbol{C} \in \mathbb{S}_+^{n_x}$, with $\mathbb{S}_+^n = \{\boldsymbol{X} \in \mathbb{S}^n \mid \boldsymbol{X} \succeq 0\}$ and $\mathbb{S}^n = \{\boldsymbol{X} \in \mathbb{R}^{n\times n} \mid \boldsymbol{X} = \boldsymbol{X}^\top\}$, be the covariance matrix of $\boldsymbol{x}(\xi)$ $\bar{\boldsymbol{x}}$ is the mean value of $\boldsymbol{x}(\xi)$. Suppose $0 < \delta \leq 0.5$. Define:

$$p^l(\boldsymbol{\xi}) = \left(\boldsymbol{h}^l\right)^\top \boldsymbol{x}(\xi) \in \mathbb{R} \tag{6}$$

which has a scalar normal probability density with mean value $\bar{p}^l = \left(\boldsymbol{h}^l\right)^\top \bar{\boldsymbol{x}}$ and variance $\sigma^{2,l} = \left(\boldsymbol{h}^l\right)^\top \boldsymbol{C}\boldsymbol{h}^l$. To make the back-off computations easier, it is convenient to normalize the stochastic process $p(\xi)$ by introducing:

$$p_n^l(\xi) := \frac{p^l(\xi) - \bar{p}^l}{\sigma^l} \tag{7}$$

then $p_n^l(\xi)$ is Gaussian with unit variance and zero mean. Then,

$$p^l(\xi) \leq g^l \Leftrightarrow \frac{p^l(\xi) - \bar{p}^l}{\sigma^l} \leq \frac{g^l - \bar{p}^l}{\sigma^l} \Leftrightarrow p_n^l(\xi) \leq \frac{g^l - \bar{p}^l}{\sigma^l} \tag{8}$$

Therefore, Eqs. (8) and (5) are replaced by:

$$\Phi\left(\frac{g^l - \bar{p}^l}{\sigma^l}\right) \geq 1-\delta^l \tag{9}$$

with Φ referring to the integration of the standard one-dimensional Gaussian distribution function to evaluate the probability:

$$\Phi(x) = \frac{1}{2\pi}\int_{-\infty}^{x} e^{-\frac{1}{2}t^2} dt \tag{10}$$

The constraint is satisfied if

$$\frac{g^l - \bar{p}^l}{\sigma^l} \geq \Phi^{-1}(1-\delta^l) \Leftrightarrow \bar{p}^l + \Phi^{-1}(1-\delta^l)\sqrt{\left(\boldsymbol{h}^l\right)^\top \boldsymbol{C}\boldsymbol{h}_l} \leq g^l \tag{11}$$

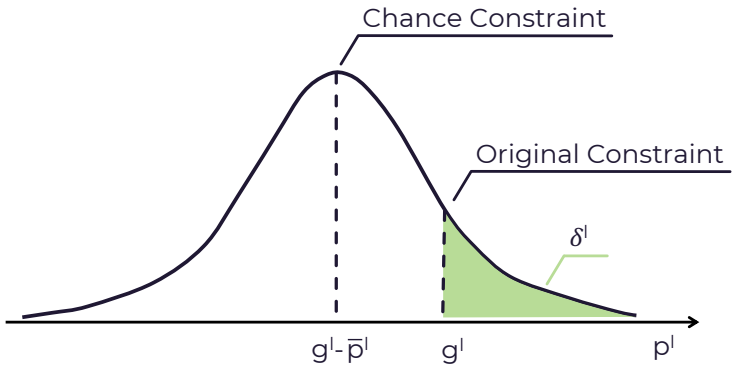

Fig. 2 Graphical representation of the 1D constraint tightening for a given δ^l.

A visual representation of the inequality condition is pictured in Fig. 2. Ultimately, a generic Non Linear Programming (NLP) problem, including chance constraints, can be framed as:

$$\min_{\boldsymbol{u}_k} \quad J(\boldsymbol{u}_k) \tag{12a}$$

$$\text{s.t.} \quad \boldsymbol{x}_{k+1} = \boldsymbol{f}(t_k, \boldsymbol{x}_k, \boldsymbol{u}_k), \tag{12b}$$

$$\bar{p}_k^l + \Phi^{-1}(1-\delta_k^l)\sqrt{(\boldsymbol{h}_k^l)^\top \boldsymbol{C}_k \boldsymbol{h}_k^l} \leq g_k^l \tag{12c}$$

Where $J : \mathbb{R}^{n_u} \to \mathbb{R}$ is a generic cost function, $f : \mathbb{R} \times \mathbb{R}^{n_x} \times \mathbb{R}^{n_u} \to \mathbb{R}^{n_x}$ is a generic discretized dynamics function, $t_k \in \mathbb{R}$ is the discretized time variable, $\boldsymbol{x}_k \in \mathbb{R}^{n_x}$ is the state, and $\boldsymbol{u}_k \in \mathbb{R}^{n_u}$ the control. In Eq. (12), k spans through all the nodes, and l identifies with the l-th constraint at each instant. The probability distribution can be propagated through nonlinear dynamics using traditional linear uncertainty propagation methods for Gaussian distributions for small initial covariance and a short time span.

$$\boldsymbol{C}_{k+1} = \boldsymbol{\Phi}_{k+1,k} \boldsymbol{C}_k \boldsymbol{\Phi}_{k+1,k}^\top \tag{13}$$

$\boldsymbol{\Phi}_{k+1,k}$ is the state transition matrix from the node k to $k+1$.

B. Iterative Risk Allocation

Iterative Risk Allocation (IRA) involves the continual adjustment of risk levels associated with chance constraints throughout the time frame of interest in the optimization. Unlike static allocation methods, iterative approaches acknowledge the evolving nature of decision problems and dynamically optimize risk parameters δ_k^l. A simple and feasible allocation for δ_k^l can be obtained by equally dividing the total allowable risk $\Delta \in \mathbb{R}_{(0,\ 0.5]}$ per node between each chance constraint. This can be written as:

$$\delta_k^l = \frac{\Delta}{N_c} \tag{14}$$

Ensuring the satisfaction of the overall chance constraint often leads to excessively conservative solutions through the prescribed risk allocation method. A more nuanced approach involves directly allocating δ_k^l within the optimization problem, resulting in a two-stage optimization framework. The upper stage, characterized by the cost function $J^*(\boldsymbol{\delta})$, focuses on solving for the risk allocation parameters δ_k^l. $J^\star(\boldsymbol{\delta})$ is the optimum objective function of the problem given set of $\boldsymbol{\delta}$:

$$\boldsymbol{\delta} = \left[\delta_1^1, \quad \cdots \quad \delta_1^{N_\mathrm{c}}, \quad \delta_2^1, \quad \cdots \quad \delta_2^{N_\mathrm{c}}, \quad \cdots \quad \delta_{N_t}^1, \quad \cdots \quad \delta_{N_t}^{N_\mathrm{c}}\right] \tag{15}$$

with N_t being the total number of time steps. The lower stage then addresses the optimization of the control problem with cost function J for a fixed value of $\boldsymbol{\delta}$ as seen in Eq. (12). The process can be reiterated until an overall solution meeting predefined tolerances is achieved. The fundamental steps of the IRA algorithm, as developed in [41], are summarized as in Alg. 1 :

1) Denoting by $\boldsymbol{\delta}_{(n)}$ the vector of unweighted risk variables δ_k^l for the n-th iteration, the IRA algorithm generates a sequence of feasible risk allocations $(\boldsymbol{\delta}_{(0)}, \boldsymbol{\delta}_{(1)}, \ldots, \boldsymbol{\delta}_{(n)})$ such that $J^*(\boldsymbol{\delta}_{(0)}) \geq J^*(\boldsymbol{\delta}_{(1)}) \geq \ldots \geq J^*(\boldsymbol{\delta}_{(n)})$.
2) Commencing with the initial feasible risk allocation $\boldsymbol{\delta}_{(n)}$, construct $\boldsymbol{\delta}'_{(n+1)}$ by tightening the inactive constraints. For each l-th active constraint, set $\left(\delta_{k,(n)}^l\right)' = \delta_{k,(n)}^l$ and for the inactive ones $\left(\delta_{k,(n)}^l\right)' < \delta_{k,(n)}^l$.
3) IRA continues by imposing $\delta_{k,(n+1)}^l = \left(\delta_{k,(n)}^l\right)'$ where the constraint is inactive. Choose then $\delta_{k,(n+1)}^l \geq \left(\delta_{k,(n)}^l\right)'$ for the active ones. This process continues iteratively until the change in the objective function resulting from the updated risk allocation falls below a specified tolerance $\epsilon_{\mathrm{IRA}} \in \mathbb{R}_+$ (i.e., $|J^*(\boldsymbol{\delta}_{(n+1)}) - J^*(\boldsymbol{\delta}_{(n)})| < \epsilon_{\mathrm{IRA}}$).

Algorithm 1 Iterative Risk Allocation

$\delta_k^l \leftarrow \Delta / N_\mathrm{c}$
while $|J^* - J^*_{\mathrm{prev}}| < \epsilon$ **do**
  $J_{\mathrm{prev}} \leftarrow J$
  Solve Problem (12) with $N_{\mathrm{active}} \leftarrow$ number of active constraints
  if $N_{\mathrm{active}} = 0$ or $N_{\mathrm{active}} = N_\mathrm{c}$ for at least one t_k **then**
    break
  end if
  for all l such that the constraint is inactive at time t_k **do**
    $\delta_k^l \leftarrow \gamma \delta_k^l + (1-\gamma)\phi\left(\dfrac{\bar{p}_k^{*l} - g_k^l}{\sqrt{\boldsymbol{h}_k^{l\top} \boldsymbol{C}_k \boldsymbol{h}_k^l}}\right)$
  end for
  $\delta_{k,\mathrm{residual}} \leftarrow \Delta - \sum_{l=1}^{N_\mathrm{c}} \delta_k^l$
  for all l such that the constraint is active at time t_k **do**
    $\delta_k^l \leftarrow \min\left(\delta_k^l + \delta_{k,\mathrm{residual}}/N_\mathrm{c},\ \epsilon_{\mathrm{IRA}}\right)$
  end for
end while

A commonly employed value for γ in Alg. 1 is 0.7 [38]. γ is a weighting parameter that determines the degree to which inactive constraints are tightened. In the combined CAM and SK, the IRA algorithm may not guarantee a reduction

in maneuver cost, especially when external constraints impact the optimality of the cost function J. Nevertheless, the approach could prove valuable during the solution process, particularly in situations where the distribution of $\boldsymbol{\delta}$ at a given iteration hinders the problem.

C. Analytical Integration of Multivariate Gaussian Distributions

In Sec. III, the SK problem will also be examined through the lens of a joint chance constraint, incorporating updates for IRA. A crucial aspect involves the analytical computation of the probability associated with an object residing within a specified ellipsoid. This section will focus on integrating a Gaussian distribution, utilizing the Square Mahalanobis Distance (SMD) as an independent variable for multidimensional distributions. Starting with the bivariate normal distribution, characterized by a mean vector $\boldsymbol{\mu} = (\mu_1, \mu_2)$ and a covariance matrix $\boldsymbol{\Sigma}$. In this context, the density function for the random variable $z = (x, y)$ is expressed as follows:

$$\mathcal{N}(z; \boldsymbol{\mu}, \boldsymbol{\Sigma}) = \frac{1}{2\pi\sqrt{|\boldsymbol{\Sigma}|}} \exp\left[-\frac{1}{2}(z-\boldsymbol{\mu})^\top \boldsymbol{\Sigma}^{-1}(z-\boldsymbol{\mu})\right] \tag{16}$$

where $\boldsymbol{\Sigma} \in \mathbb{S}^2_{++}$ with $\mathbb{S}^n_{++} = \{\boldsymbol{X} \in \mathbb{S}^n \mid \boldsymbol{X} \succ 0\}$. To compute the integral of the Gaussian, suppose without loss of generality that $\boldsymbol{\mu} = \mathbf{0}$ (since integrals are invariant under translation). Thus, the desired cumulative function is given by (please find the full derivation in [42]):

$$F(d) = 1 - e^{-\frac{d^2}{2}} \tag{17}$$

with d being the Mahalanobis distance. Eq. (17) is invertible, and its inverse can be computed explicitly. In other words, if the probability p that a point is within Mahalanobis distance d from the Gaussian is known, then d is:

$$d = F^{-1}(p) = \sqrt{-2\ln(1-p)} \tag{18}$$

If interested, the reader can find the n-dimensional case is analyzed in [42].

D. Gaussian quadrature for quadrilateral elements

Gaussian quadrature is a numerical integration method relevant to finite element analysis, specifically tailored for quadrilateral elements. By strategically placing integration points and weights, Gaussian quadrature facilitates precise and efficient numerical integration over complex domains. Conforming to the joint constraint analysis, Gaussian quadrature will be strategically utilized to integrate a multidimensional Gaussian distribution over a rectangular domain in Sec. III.

Gaussian quadrature typically operates on the quadrilateral element $R_{\text{st}} = [-1, 1]^2$. The integral over R_{st} is then

[43]:

$$I = \iint_{R_{\text{st}}} g(\xi, \eta)\, d\xi\, d\eta = \int_{-1}^{1} \int_{-1}^{1} g(\xi, \eta)\, d\xi\, d\eta \approx \sum_{i=1}^{M} \sum_{j=1}^{N} w_i \tilde{w}_j g(\xi_i, \eta_j) \tag{19}$$

Here, ξ_i and η_j represent the Gaussian quadrature points, while w_i and $\tilde{w}_j$ denote the corresponding weights. The accuracy of this integration method is contingent on N and M; greater values enhance it, at the cost of increased computational burden. For a general rectangular domain $R_{\text{g}} = [a, b] \times [c, d]$ with $a \leq b$, $c \leq d$ and $a, b, c, d \in \mathbb{R}$. Eq. (19) changes to:

$$\iint_{R_{\text{g}}} F(x, y)\, dx\, dy \approx \frac{b-a}{2} \frac{d-c}{2} \sum_{i=1}^{M} \sum_{j=1}^{N} w_i \widetilde{w}_j F\left(a + \frac{b-a}{2}(1+\xi_i),\ c + \frac{d-c}{2}(1+\eta_j)\right), \tag{20}$$

The weights are commonly precomputed and tabulated for various numbers of nodes. Alternatively, if needed, specific algorithms are available to calculate and store these weights in advance for any N or M [44]. They are retrieved during the evaluation of integrals, reducing the computational effort required.

III. Mathematical Framework

A. Optimization Problem Setup

Consider two spacecraft, denoted as primary and secondary, with positions and velocities in an Earth-Centered Inertial (ECI) reference frame (r.f.) at time t_0. These attributes are modeled as Gaussian multivariate random variables:

$$\boldsymbol{x}_{\text{p}}(t_0) \sim \mathcal{N}(\boldsymbol{\mu}_{\text{p}}(t_0), \boldsymbol{C}_{\text{p}}(t_0)), \qquad \boldsymbol{x}_{\text{s}}(t_0) \sim \mathcal{N}(\boldsymbol{\mu}_{\text{s}}(t_0), \boldsymbol{C}_{\text{s}}(t_0)) \tag{21}$$

$\boldsymbol{x}_{\text{p}}(t_0), \boldsymbol{x}_{\text{s}}(t_0) \in \mathbb{R}^6$ represent positions and velocities, and $\boldsymbol{\mu}_{\text{p}}(t_0), \boldsymbol{\mu}_{\text{s}}(t_0) \in \mathbb{R}^6$ are their mean values, with covariance matrices $\boldsymbol{C}_{\text{p}}(t_0), \boldsymbol{C}_{\text{s}}(t_0) \in \mathbb{S}^6_{++}$. Additionally, a control acceleration $\boldsymbol{u}(t) \in \mathbb{R}^3$ acts on the primary satellite. All variables and dynamics are scaled for numerical stability according to Table 1.

Table 1 Scaling parameters

Parameter	Value	Unit
Earth gravitational constant ($\mu_{\oplus}$)	398600.4418	$\left[\text{km}^3/\text{s}^2\right]$
Earth radius scaling constant (L_{sc})	6378.173	[km]
Velocity scaling constant (V_{sc})	$\sqrt{\frac{\mu_{\oplus}}{L_{\text{sc}}}}$	[km/s]
Time scaling constant (T_{sc})	$\frac{L_{\text{sc}}}{V_{\text{sc}}}$	[s]
Acceleration scaling constant (A_{sc})	$\frac{V_{\text{sc}}}{T_{\text{sc}}}$	$\left[\text{km}/\text{s}^2\right]$

The mean state and covariance evolution of both objects follows a numerical propagation determined by dynamical models:

$$\boldsymbol{l}_{\mathrm{p}}(t, \boldsymbol{\mu}_{\mathrm{p}}(t), \boldsymbol{u}, \boldsymbol{p}_{\mathrm{p}}, \boldsymbol{C}_{\mathrm{p},0}, \boldsymbol{\mu}_{\mathrm{p},0}) = \begin{cases} \dot{\boldsymbol{\mu}}_{\mathrm{p}}(t) = \boldsymbol{f}_{\mathrm{p}}(t, \boldsymbol{\mu}_{\mathrm{p}}(t), \boldsymbol{u}, \boldsymbol{p}_{\mathrm{p}}) \\ \boldsymbol{C}_{\mathrm{p}}(t) = \boldsymbol{A}_{\mathrm{s}}(t,\ t_0)\boldsymbol{C}_{\mathrm{p}}(t_0)\boldsymbol{A}_{\mathrm{p}}(t,\ t_0)^{\top} \\ \dot{\boldsymbol{A}}_{\mathrm{p}}(t,\ t_0) = \boldsymbol{B}_{\mathrm{p}}(t)\boldsymbol{A}_{\mathrm{p}}(t,\ t_0) \qquad \text{with } \boldsymbol{B}_{\mathrm{p}}(t) = \left.\dfrac{\partial \boldsymbol{f}_{\mathrm{p}}(t, \boldsymbol{x}_{\mathrm{p}}(t), \boldsymbol{u}, \boldsymbol{p}_{\mathrm{p}})}{\partial \boldsymbol{x}_p}\right|_{\boldsymbol{x}_p = \boldsymbol{\mu}_{\mathrm{p}}} \\ \boldsymbol{\mu}_{\mathrm{p}}(t_0) = \boldsymbol{\mu}_{\mathrm{p},0} \\ \boldsymbol{C}_{\mathrm{p}}(t_0) = \boldsymbol{C}_{\mathrm{p},0} \end{cases} \tag{22}$$

$$\boldsymbol{l}_{\mathrm{s}}(t, \boldsymbol{\mu}_{\mathrm{s}}(t), \boldsymbol{p}_{\mathrm{s}}, \boldsymbol{C}_{\mathrm{s},0}, \boldsymbol{\mu}_{\mathrm{s},0}) = \begin{cases} \dot{\boldsymbol{\mu}}_{\mathrm{s}}(t) = \boldsymbol{f}_{\mathrm{s}}(t, \boldsymbol{\mu}_{\mathrm{s}}(t), \boldsymbol{p}_{\mathrm{s}}) \\ \boldsymbol{C}_{\mathrm{s}}(t) = \boldsymbol{A}_{\mathrm{s}}(t,\ t_0)\boldsymbol{C}_{\mathrm{s}}(t_0)\boldsymbol{A}_{\mathrm{s}}(t,\ t_0)^{\top} \\ \dot{\boldsymbol{A}}_{\mathrm{s}}(t,\ t_0) = \boldsymbol{B}_{\mathrm{s}}(t)\boldsymbol{A}_{\mathrm{s}}(t,\ t_0) \qquad \text{with } \boldsymbol{B}_{\mathrm{s}}(t) = \left.\dfrac{\partial \boldsymbol{f}_{\mathrm{s}}(t, \boldsymbol{x}_{\mathrm{s}}(t), \boldsymbol{p}_{\mathrm{s}})}{\partial \boldsymbol{x}_s}\right|_{\boldsymbol{x}_s = \boldsymbol{\mu}_{\mathrm{s}}} \\ \boldsymbol{\mu}_{\mathrm{s}}(t_0) = \boldsymbol{\mu}_{\mathrm{s},0} \\ \boldsymbol{C}_{\mathrm{s}}(t_0) = \boldsymbol{C}_{\mathrm{s},0} \end{cases} \tag{23}$$

In Eq. (22), (23), $\boldsymbol{f}_{\mathrm{p/s}}$ relate to the primary and secondary spacecraft, respectively. $t \in \mathbb{R}_{[t_0,t_{\mathrm{f}}]}$ links to the simulation time domain, $\boldsymbol{p}_{\mathrm{p}} \in \mathbb{R}^{m_{\mathrm{p}}}$ and $\boldsymbol{p}_{\mathrm{s}} \in \mathbb{R}^{m_{\mathrm{s}}}$ depict the sets of parameters. Functions $\boldsymbol{f}_{\mathrm{p}} : \mathbb{R}_{[t_0,t_{\mathrm{f}}]} \times \mathbb{R}^6 \times \mathbb{R}^3 \times \mathbb{R}^{m_{\mathrm{p}}} \to \mathbb{R}^6$ and $\boldsymbol{f}_{\mathrm{s}} : \mathbb{R}_{[t_0,t_{\mathrm{f}}]} \times \mathbb{R}^6 \times \mathbb{R}^{m_{\mathrm{s}}} \to \mathbb{R}^6$ are continuous. $\boldsymbol{A}_{\mathrm{p/s}}(t,\ t_0)$ denotes the STM of the objects from time t_0 to t, $\boldsymbol{B}_{\mathrm{p/s}}(t)$ represents the related state matrix, and $\boldsymbol{\mu}_{\mathrm{p/s},0}$ and $\boldsymbol{C}_{\mathrm{p/s},0}$ are the initial mean states and covariance matrices. It is worth noting that $\boldsymbol{l}_{\mathrm{s}}$ is propagated only once since the secondary object lacks control acceleration, whilst $\boldsymbol{l}_{\mathrm{p}}$ it occcurs multiple times inside the optimization pipeline.

In Sec. IV, the Accurate Integrator for Debris Analysis (AIDA), presented in reference [45], is used to determine the dynamics evolution of the bodies. It incorporates the following acceleration vector:

$$\boldsymbol{a}_{\mathrm{AIDA}} = \boldsymbol{a}_{♁} + \boldsymbol{a}_{☼} + \boldsymbol{a}_{☾} + \boldsymbol{a}_{\mathrm{SRP}}, \tag{24}$$

$\boldsymbol{a}_{♁}$ is the Earth's gravitational pull, computed using a potential model of order up to 10. $\boldsymbol{a}_{☼}$ and $\boldsymbol{a}_{☾}$ represent the third body accelerations of the Sun and Moon, calculated with NASA's SPICE toolkit [46]. Finally, $\boldsymbol{a}_{\mathrm{SRP}}$ is SRP, derived using a dual-cone shadow model and assuming a cannonball geometry for the spacecraft.

The Gaussian nature of variables is retained if nonlinearities are confined within the considered uncertainty set, especially in short propagation windows and for small initial covariances. In defining the CAM requirement, it is vital to explicitly state the relative position of the primary object to each secondary:

$$\delta \boldsymbol{r}_{\mathrm{s}}(t) = \boldsymbol{r}_{\mathrm{p}}(t) - \boldsymbol{r}_{\mathrm{s}}(t), \quad \text{with } \boldsymbol{r}_{\mathrm{p}} = \boldsymbol{x}_{\mathrm{p},1:3},\ \boldsymbol{r}_{\mathrm{s}} = \boldsymbol{x}_{\mathrm{s},1:3} \tag{25}$$

Given that subtraction is a linear transformation, the relative position is also normally distributed:

$$\delta \boldsymbol{r}_{\mathrm{s}}(t) \sim \mathcal{N}\big(\boldsymbol{\mu}_{\mathrm{p},1:3}(t) - \boldsymbol{\mu}_{\mathrm{s},1:3}(t), \boldsymbol{P}^{\mathrm{TOT}}(t)\big), \quad \boldsymbol{P}^{\mathrm{TOT}}(t) = \boldsymbol{C}_{\mathrm{p},1:3,1:3}(t) + \boldsymbol{C}_{\mathrm{s},1:3,1:3}(t) \tag{26}$$

The relative distance, together with the combined hard body radius, is used to define IPoC, indicated as $P_{IC} \in \mathbb{R}_{(0,1)}$. The details of the computation of IPoC are omitted here for conciseness but can be found in [15]. It suffices to say that an inequality constraint must be respected at all times, bounding the maximum value of IPoC. Turning to the stochastic SK constraint, it reads as the individual probabilities $1 - \delta$ of the primary to stay within a rectangular domain $\mathrm{R}_{\mathrm{SK}} = [\lambda_{\min}, \lambda_{\max}] \times [\phi_{\min}, \phi_{\max}]$ for every node with λ being the longitude and ϕ the latitude.

Therefore, the standard Optimal Control Problem (OCP) in the continuous domain for the long-term conjunction CAM and stochastic SK problem is stated as follows:

$$\min_{\boldsymbol{u}(t)} \quad J = \int_{t_0}^{t_{\mathrm{f}}} u(t)\mathrm{d}t, \tag{27a}$$

$$\text{s.t.} \quad \boldsymbol{l}_{\mathrm{p}}(t, \boldsymbol{\mu}_{\mathrm{p}}(t), \boldsymbol{u}(t), \boldsymbol{p}_{\mathrm{p}}, \boldsymbol{C}_{\mathrm{p},0}, \boldsymbol{\mu}_{\mathrm{p},0}) \tag{27b}$$

$$P_{IC}(t, \delta \boldsymbol{r}_{\mathrm{s}}(t)) \leq \bar{P}_{IC} \tag{27c}$$

$$\Pr(\boldsymbol{r}_{\mathrm{p}}(t) \mid \lambda(\boldsymbol{r}_{\mathrm{p}}(t)) \leq \lambda_{\max}) \leq 1 - \delta \tag{27d}$$

$$\Pr(\boldsymbol{r}_{\mathrm{p}}(t) \mid \lambda(\boldsymbol{r}_{\mathrm{p}}(t)) \geq \lambda_{\min}) \leq 1 - \delta \tag{27e}$$

$$\Pr(\boldsymbol{r}_{\mathrm{p}}(t) \mid \phi(\boldsymbol{r}_{\mathrm{p}}(t)) \leq \phi_{\max}) \leq 1 - \delta \tag{27f}$$

$$\Pr(\boldsymbol{r}_{\mathrm{p}}(t) \mid \phi(\boldsymbol{r}_{\mathrm{p}}(t)) \geq \phi_{\min}) \leq 1 - \delta \tag{27g}$$

$$u(t) = ||\boldsymbol{u}(t)||, \tag{27h}$$

$$u(t) \leq u_{\max} \tag{27i}$$

Eq. (27a) aims at minimizing the overall control effort. A set of diverse constraints constitutes the optimization problem: Eq. (27b) encapsulates the evolution of the primary state variables under a control acceleration $\boldsymbol{u}(t)$. Equation (27c) delineates the IPoC constraint, rigorously enforced at each integration node; the evolution of the secondary's mean state and covariance determines the evolution of IPoC. Eq. (27d)-(27g) quantify ($\Pr \in \mathbb{R}_{(0,0.5]}$) the instantaneous probability of the primary not existing a SK box thanks to individual chance constraints, characterized by sharp longitude and latitude boundaries; δ is the so-called violation probability. Eq. (27i) imposes an upper bound on the magnitude of the instantaneous control action. The mass variation is neglected given the expected low value of the Δv.

B. Problem Convexification

Eqs. (27b)-(27i) are transformed to be used in a SCP class following [15]. SCP systematically approximates the global solution of the OCP through a Second-order Cone Program (SOCP). The constraints and the objective function are revisited and adjusted to accommodate all the requirements given three sources of non-convexity:

1) The dynamics in Eq. (27b) are in general nonlinear.

2) Eq (27c) is a nonlinear constraint. The same holds from Eq. (27d) to Eq. (27g).

3) Both Eq (27a) and Eq (27h) pose challenges for achieving a feasible objective function within a SOCP framework.

The problem is initially subjected to discretization. The simulation time domain, expressed as $t \in \mathbb{R}_{[t_0,t_f]}$, is discretized into a set of time instances $t_i \in \{t_0, t_1, ..., t_N\}$, where $N+1$ signifies the number of nodes. Adopting an integration technique such as Runge-Kutta 7-8 and including the geopotential, Lunisolar, and SRP perturbations, the states of the two spacecraft at t_i are determined. Based on a SCP, the optimization is subjected to successive linearization identified with the index j.

A significant portion of the constraints convexification has been extensively discussed in previous works by Z. Pavanello et al. in [19] and [15] and only recalled here for conciseness. In synthesis, the dynamics constraint in Eq. (27b) is automatically linearized; the IPoC constraint in Eq. (27c) is first turned into a SMD constraint and successively linearized using a projection and linearization algorithm; the fuel-optimal objective function in Eq. (27a) is taken care of by introducing a second-order cone on the control acceleration. The overall pipeline, including the Chance Constrained Station-Keeping (CCSK) described later in this section, is drafted in Fig. 3. The reader should note that while the condition stipulated by the IRA algorithm, $J^*(\boldsymbol{\delta}_{(0)}) \geq J^*(\boldsymbol{\delta}_{(1)}) \geq \ldots \geq J^*(\boldsymbol{\delta}_{(n)})$, is significant, it may not be fully applicable in this context. Other constraints beyond the mere SK can influence the evolution of the cost function J. In this case, the overall indication of the convergence hinges on the disparity between the propagated and linearized orbit.

1. Individual chance constraint formulation for the station keeping problem

Maneuvers in GEO must adhere to a SK constraint, conceptualized as a "keep-in box" in two dimensions: the longitude and latitude of the spacecraft. The nonlinear dynamics governing the evolution of the two geodetic variables $\boldsymbol{\gamma} = [\lambda,\ \phi]^\top$ depend solely on the state of the primary spacecraft and the time variable:

$$\boldsymbol{\gamma}(t) = \boldsymbol{g}(t, \boldsymbol{\mu}_{\mathrm{p}}(t)) \tag{28}$$

where $\boldsymbol{g}(\cdot) : \mathbb{R}[t_0, t_f] \times \mathbb{R}^6 \rightarrow \mathbb{R}^2$ is a function that transforms the state into Earth-Centered Earth Fixed (ECEF) and then into geodetic coordinates, and $\boldsymbol{\gamma}(t) \in \mathbb{R}^2$ is the vector comprising latitude and longitude. Eq. (28) approximates as a first-order Taylor polynomial ($\mathcal{T}_{\boldsymbol{\gamma}}^1$):

$$\boldsymbol{\gamma}_i^j = \mathcal{T}_{\boldsymbol{\gamma}_i^j}^1(\boldsymbol{\mu}_{\mathrm{p},i}^j), \quad i \in \{1,\ ...,\ N\} \tag{29}$$

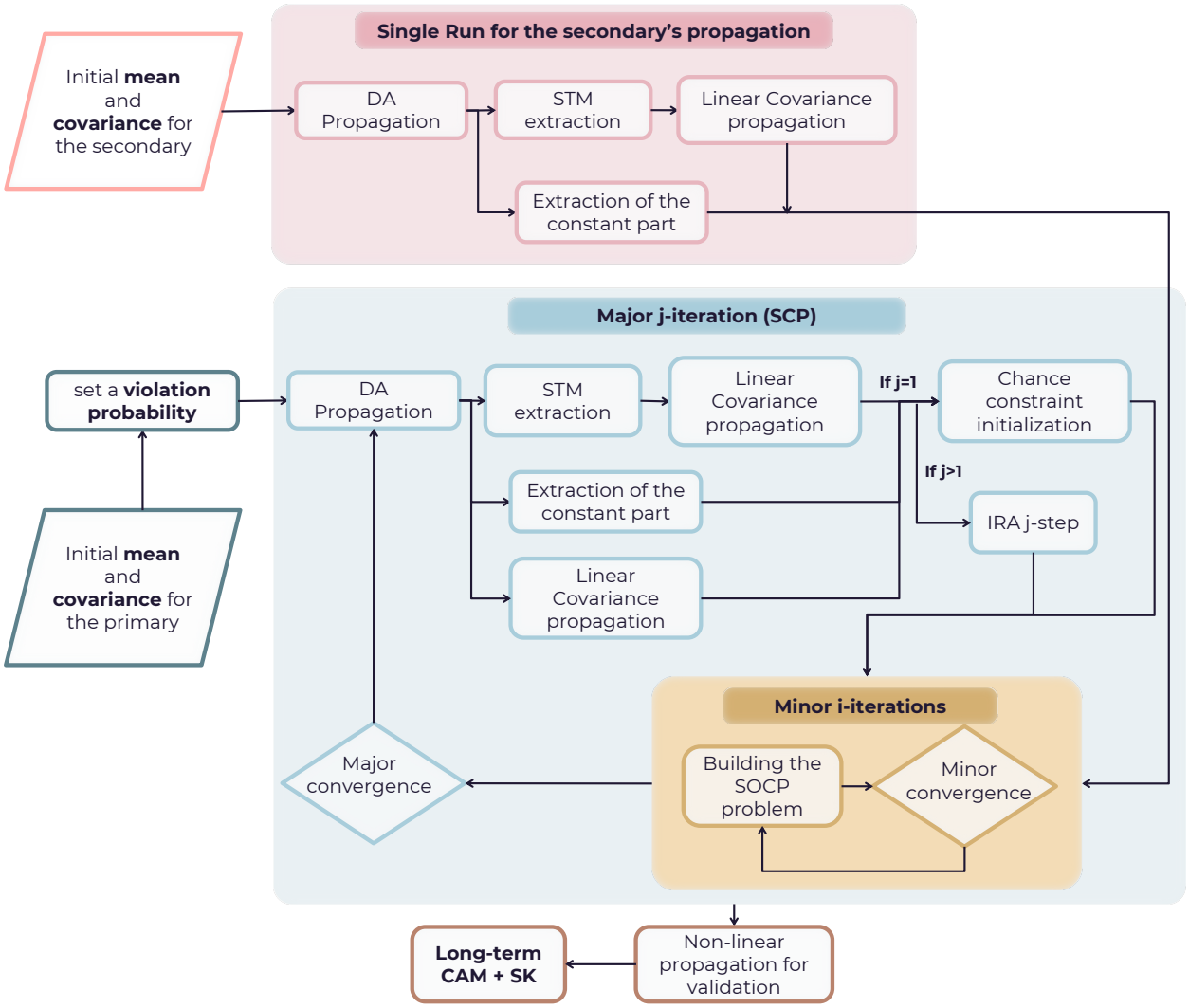

Fig. 3 Flowchart summarizing the embedded CAM and SK pipeline.

Eq. (29) embeds the geodetic coordinate variations as a linear transformation dependent on the perturbations of the state vector:

$$\delta\boldsymbol{\gamma}_i^j = \boldsymbol{G}_i^j \delta\boldsymbol{\mu}_{\mathrm{p},i}^j, \quad i \in \{1, \ldots, N\} \tag{30}$$

where $\boldsymbol{G}_i^j \in \mathbb{R}^{2\times 6}$ is the linear map of the geodetic transformation for node i in major iteration j. The SK requirement specifies that latitude and longitude must remain within a rectangular box throughout the simulation time window. The box is centered on the nominal coordinates $\boldsymbol{\gamma}_0 \in \mathbb{R}^2$, with its dimensions determined by the elements of $\Delta\boldsymbol{\gamma} \in \mathbb{R}^2$.

$$\boldsymbol{\gamma}_0 - \Delta\boldsymbol{\gamma} \preceq \boldsymbol{\gamma}_i^j \preceq \boldsymbol{\gamma}_0 + \Delta\boldsymbol{\gamma}, \quad i \in \{1, \ldots, N\} \tag{31}$$

Here, $\preceq$ indicates the componentwise inequality. Up to now, no information on the state uncertainty has been provided for the SK chance constraint. The covariance $\boldsymbol{C}_{p,i}^{j}$ of the primary in ECI is ready available with a linear uncertainty propagation and can be transposed into the equivalent ECEF r.f.:

$$\boldsymbol{C}_{p,i}^{ECEF,j} = \boldsymbol{R}_{ECI\rightarrow ECEF,i}^{j} \boldsymbol{C}_{p,i}^{j} (\boldsymbol{R}_{ECI\rightarrow ECEF,i}^{j})^{\top} \tag{32}$$

$\boldsymbol{R}_{ECI\rightarrow ECEF,i}^{j}$ is computed via SPICE toolkit [46]. By extracting only the position sub-covariance matrix $\boldsymbol{P}_{p,i}^{ECEF,j}$ from $\boldsymbol{C}_{p,i}^{ECEF,j}$, the equivalent description in spherical coordinates (λ, ϕ, ρ) corresponding to latitude, longitude and altitude:

$$\boldsymbol{P}_{p,i}^{SPH,j} = \boldsymbol{J}_{ECEF\rightarrow SPH,i}^{j} \boldsymbol{P}_{p,i}^{ECEF,j} (\boldsymbol{J}_{ECEF\rightarrow SPH,i}^{j})^{\top} \tag{33}$$

$\boldsymbol{J}_{ECEF\rightarrow SPH,i}^{j} \in \mathbb{R}^{3\times 3}$ associates with the jacobian transformation matrix from the position covariance. The variance information on λ and ϕ is:

$$\sigma_{\lambda,i}^{j} = \sqrt{\boldsymbol{P}_{p,i,(1,1)}^{SPH,j}}, \quad \sigma_{\phi,i}^{j} = \sqrt{\boldsymbol{P}_{p,i,(2,2)}^{SPH,j}} \tag{34}$$

They are organized into $\boldsymbol{\sigma}_{\boldsymbol{\gamma},i}^{j} = [\sigma_{\lambda,i}^{j},\ \sigma_{\phi,i}^{j}]^{\top}$ and bounds are defined as

$$\begin{aligned} \boldsymbol{h}_{\mathrm{inv},i}^{\mathrm{up},j} &= [\Phi^{-1}(1-\delta_{\lambda,i}^{\mathrm{up},j}),\ \Phi^{-1}(1-\delta_{\phi,i}^{\mathrm{up},j})]^{\top} \\ \boldsymbol{h}_{\mathrm{inv},i}^{\mathrm{lo},j} &= [\Phi^{-1}(1-\delta_{\lambda,i}^{\mathrm{lo},j}),\ \Phi^{-1}(1-\delta_{\phi,i}^{\mathrm{lo},j})]^{\top} \end{aligned} \tag{35}$$

where Φ^{-1} is the Normal Inverse Cumulative Distribution Function, and the superscripts "up" and "lo" stand for upper and lower boundaries. The SK chance constraint from Sec. II.A can be stated as:

$$\boldsymbol{G}_{i}^{j} \boldsymbol{\mu}_{\mathrm{p},i}^{j} + \boldsymbol{v}_{\mathrm{sk},i}^{j} \succeq \boldsymbol{\gamma}_{0} - \Delta\boldsymbol{\gamma} + \boldsymbol{\sigma}_{\boldsymbol{\gamma},i}^{j} \circ \boldsymbol{h}_{\mathrm{inv},i}^{\mathrm{lo},j} + \boldsymbol{d}_{i}^{j} \qquad \text{for } i \in \{1,\ ...,\ N\} \tag{36a}$$

$$\boldsymbol{G}_{i}^{j} \boldsymbol{\mu}_{\mathrm{p},i}^{j} + \boldsymbol{v}_{\mathrm{sk},i}^{j} \preceq \boldsymbol{\gamma}_{0} + \Delta\boldsymbol{\gamma} - \boldsymbol{\sigma}_{\boldsymbol{\gamma},i}^{j} \circ \boldsymbol{h}_{\mathrm{inv},i}^{\mathrm{up},j} + \boldsymbol{d}_{i}^{j}, \qquad \text{for } i \in \{1,\ ...,\ N\} \tag{36b}$$

where $\boldsymbol{d}_{i}^{j} = \boldsymbol{G}_{i}^{j} \boldsymbol{\mu}_{\mathrm{p},i}^{j-1} - \tilde{\boldsymbol{\gamma}}_{i}^{j}$ is the residual of the linearization and $\tilde{\boldsymbol{\gamma}}_{i}^{j} = \boldsymbol{g}(\tilde{\boldsymbol{\mu}}_{\mathrm{p},i}^{j}, t_i)$ is the constant part of the geodetic transformation, i.e., the nonlinear function evaluation of the expansion point $(\tilde{\boldsymbol{\mu}}_{\mathrm{p},i}^{j}, t_i)$, and $\circ$ is the Hadamard product. $\boldsymbol{v}_{sk,i}^{j} \in \mathbb{R}^{2}$ refers to the virtual buffer for the station-keeping constraint to counteract additional trust region constraints essential for managing linearized nonlinear problems. A full description is here omitted for the sake of conciseness; one can find more insights in [15] [19] [22] [26] [27] . The idea is to incorporate a node-wise constraint, restricting the norm of the maximum legitimate deviation in state variables concerning the linearization point. Of significance, $\boldsymbol{\sigma}_{\boldsymbol{\gamma},i}^{j}$ is prone to increase over time, especially in the λ direction; the upper and lower bounds may intersect, rendering the maneuver design unfeasible. If $j > 1$ with one or more active constraints, the IRA shown in Sec. II.B reassignes the

value of δ and consequently of $\boldsymbol{h}^{\mathrm{lo},j}_{inv,i}$ and $\boldsymbol{h}^{\mathrm{up},j}_{inv,i}$ to all the involved nodes.

C. Final form of the SOCP with individual SK chance constraints

The same procedure for including the virtual controls is applied in the linearized dynamical evolution [15]

$$\boldsymbol{\mu}^{j}_{\mathrm{p},i+1} + \boldsymbol{\nu}^{j}_{\mathrm{dyn},i} = \boldsymbol{A}^{j}_{\mathrm{p},i+1}\boldsymbol{\mu}^{j}_{i} + \boldsymbol{B}^{j}_{i+1}\boldsymbol{u}^{j}_{i} + \boldsymbol{c}^{j}_{i} \quad \text{for } i \in \{0, N-1\}, \quad \text{with} \quad \boldsymbol{c}^{j}_{i} = \tilde{\boldsymbol{\mu}}^{j}_{\mathrm{p},i+1} - \boldsymbol{A}^{j}_{\mathrm{p},i+1}\tilde{\boldsymbol{\mu}}^{j}_{i} - \boldsymbol{B}^{j}_{i+1}\boldsymbol{u}^{j}_{i} \tag{37}$$

The virtual controls are minimized via a node-wise second-order cone[15]:

$$\nu_i \geq \sqrt{\|\boldsymbol{\nu}^{j}_{\mathrm{dyn},i}\|^2 + \|\boldsymbol{\nu}^{j}_{sk,i}\|^2}, \quad \text{for } i \in \{1,\ \ldots,\ N\} \tag{38a}$$

$$J_{vc} = \kappa_{\nu_c} \sum_{i=0}^{N} \nu_i \tag{38b}$$

Ultimately, the complete objective function is given by the sum of the fuel-optimal and the virtual control terms:

$$J = \sum_{i=0}^{N-1} u_i \cdot \Delta t_i + J_{vc} \tag{39}$$

where $\Delta t_i \in \mathbb{R}_+$ is the time interval between nodes i and $i+1$.

The final SOCP is reported then

$$\begin{aligned} \min_{\boldsymbol{\mu}_p, \boldsymbol{u}, \boldsymbol{\nu}} \quad & \text{Eq. (39)} \\ \text{s.t.} \quad & \text{Eqs. (22), (36a), (36b), (37), (38a)} \\ & \text{Eqs. (25a), (27), (29), (59), (60b) from [15].} \end{aligned} \tag{40}$$

The full history of state and controls is expressed with the symbols $\boldsymbol{M} \in \mathbb{R}^{6(N+1)}$ and $\boldsymbol{U} \in \mathbb{R}^{3N}$:

$$\boldsymbol{M} = \begin{bmatrix} \boldsymbol{\mu}_0^T & \boldsymbol{\mu}_1^T & \cdots & \boldsymbol{\mu}_N^T \end{bmatrix}^T, \quad \boldsymbol{U} = \begin{bmatrix} \boldsymbol{u}_0^T & \boldsymbol{u}_1^T & \cdots & \boldsymbol{u}_{N-1}^T \end{bmatrix}^T \tag{41}$$

As illustrated in Fig. 3, both the minor and major iterations depend on convergence criteria. Specifically, the user must define the maximum number of iterations for the two loops and the allowable maximum control and position error $(\tau_{\mathrm{maj}},\ \tau_{\mathrm{min}})$ between two consecutive iterations to check convergence:

$$\varepsilon^{j}_{i,\mathrm{cntrl}} = \|\boldsymbol{u}^{j}_{i} - \boldsymbol{u}^{j-1}_{i}\| \quad \text{for} \quad i = 1, \ldots N; \tag{42}$$

The maximum control error from $j-1$ to j is:

$$\tilde{\varepsilon}^{j}_{\text{cntrl}} = \max(\boldsymbol{\varepsilon}^{j}_{\text{cntrl}} \cdot c_{\text{cntrl}}) \quad \text{convergence if} \quad \tilde{\varepsilon}^{j}_{\text{cntrl}} < \tau_{\text{maj}} \tag{43}$$

Where c_{cntrl} is a control coefficient scaling factor. Similarly, for the minor iteration, check the relative position:

$$\varepsilon^{j}_{\text{pos},k,i} = \|\boldsymbol{\mu}^{j}_{k,i,1:3} - \boldsymbol{\mu}^{j}_{k+1,i,1:3}\| \quad \text{for} \quad i = 1, \dots N; \tag{44}$$

$$\tilde{\varepsilon}^{j}_{\text{pos},k} = \max(\boldsymbol{\varepsilon}^{j}_{\text{pos},k}) \quad \text{convergence if} \quad \tilde{\varepsilon}^{j}_{\text{pos},k} < \tau_{\text{min}} \tag{45}$$

Equation (43) pertains to a major iteration step, while Eq. (45) applies to minor iteration steps, where k denotes the minor iteration index.

D. Joint SK Chance Constraint

As outlined in Sec. II.A, joint chance constraints are essential for satisfying linear inequalities with a specified violation probability δ. However, incorporating them into an optimization problem is not as straightforward as their individual counterparts due to the intricate stochastic interconnections. This section will introduce an approach to managing joint chance constraints within rectangular keep-in or keep-out domains that are scalable to higher dimensions. Consider a scenario where a satellite needs to simultaneously satisfy chance constraints for both longitude and latitude, such as:

$$\Pr(\boldsymbol{r}_{\text{p}}(t) \mid \lambda_{\text{min}} \leq \lambda(\boldsymbol{r}_{\text{p}}(t)) \leq \lambda_{\text{max}}, \phi_{\text{min}} \leq \phi(\boldsymbol{r}_{\text{p}}(t)) \leq \phi_{\text{max}}) \leq 1-\delta \tag{46}$$

If the assumption of 2D Gaussian PDF holds true for the simulation time window, from Eq. (18) in Sec. II.C, when considering a generic linearization step j and a node i:

$$d_i^j = \sqrt{-2\ln(\delta_i^j)}. \tag{47}$$

where d_i^j is the Mahalanobis Distance of an ellipse with probability $1-\delta_i^j$ of enclosing the primary at a specific time step. Let us drop the indices i and j to streamline notation and recover it in the final joint constraint formulation. By recalling the definition of SMD and by defining the variables $\bar{\lambda} = \lambda - \mu_\lambda,\ \bar{\phi} = \phi - \mu_\phi$:

$$\frac{1}{1-\rho^2}\left(\frac{\bar{\lambda}^2}{\sigma_\lambda^2} - \frac{2\rho\bar{\lambda}\bar{\phi}}{\sigma_\lambda\sigma_\phi} + \frac{\bar{\phi}^2}{\sigma_\phi^2}\right) = d^2 \rightarrow a\bar{\lambda}^2 + b\bar{\lambda}\bar{\phi} + c\bar{\phi}^2 = d^2 \tag{48}$$

$\rho \in (0,1)$ characterizes the degree of correlation and $a, c \in \mathbb{R}_+$, $b \in \mathbb{R}$ are the coefficients of a generic ellipse equation in $\bar{\lambda}, \bar{\phi}$. The present objective is to identify a rectangular domain R_{mid} such that the probability of encapsulating the

spacecraft precisely equals $1-\delta$, as depicted in Fig. 4. The r.f. is centered on the primary at each i-th node. The domain confined by the ellipse with a light green edge features a probability of $1-\delta$ to contain the spacecraft. The darker green rectangle is an equivalent domain with the same probability $1-\delta$. This shift in perspective is motivated by

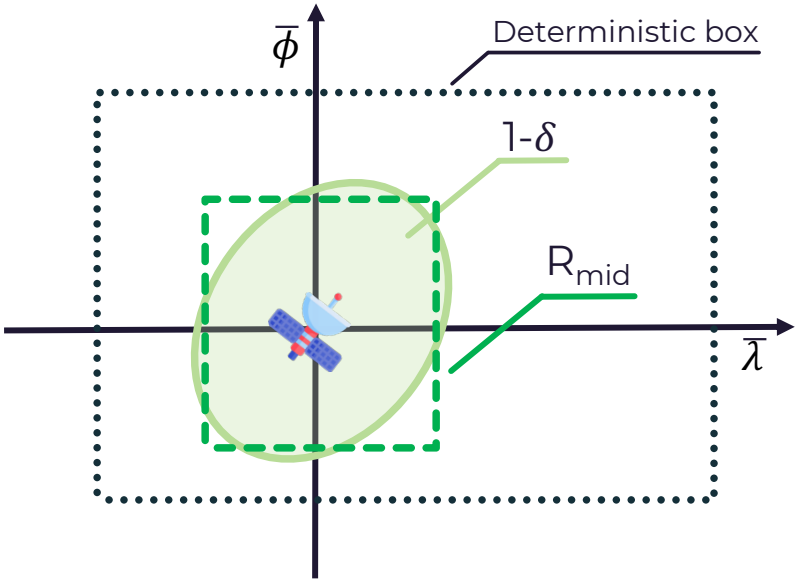

Fig. 4 Joint SK representation over a rectangular domain.

the forthcoming update in the IRA algorithm, specifically tailored for constraints with a rectangular geometry. In the literature, there is no known explicit integral of a Gaussian PDF for such geometries, making the problem seemingly intractable at first glance. A possible solution is finding two rectangular domains $\mathrm{R}_{\mathrm{outer}}$ and $\mathrm{R}_{\mathrm{inner}}$ such that:

$$\Pr(\boldsymbol{r}_{\mathrm{p}} \mid (\lambda(\boldsymbol{r}_{\mathrm{p}}), \phi(\boldsymbol{r}_{\mathrm{p}})) \in \mathrm{R}_{\mathrm{outer}}) \geq 1-\delta, \quad \Pr(\boldsymbol{r}_{\mathrm{p}} \mid (\lambda(\boldsymbol{r}_{\mathrm{p}}), \phi(\boldsymbol{r}_{\mathrm{p}})) \in \mathrm{R}_{\mathrm{inner}}) \leq 1-\delta \tag{49}$$

and, by iterating with a bisection-like algorithm, get $\mathrm{R}_{\mathrm{mid}}$:

$$\Pr(\boldsymbol{r}_{\mathrm{p}} \mid (\lambda(\boldsymbol{r}_{\mathrm{p}}), \phi(\boldsymbol{r}_{\mathrm{p}})) \in \mathrm{R}_{\mathrm{mid}}) = 1-\delta \tag{50}$$

The coordinates of $\mathrm{R}_{\mathrm{outer}}$ are computed by intersecting the SMD equation with lines parallel to the axes $\bar{\lambda}, \bar{\phi}$ as displayed in Fig. 5.

$$\begin{cases} a\bar{\lambda}^2 + b\bar{\lambda}\bar{\phi} + c\bar{\phi}^2 = d^2 \\ \bar{\lambda} = k \end{cases} \qquad \begin{cases} a\bar{\lambda}^2 + b\bar{\lambda}\bar{\phi} + c\bar{\phi}^2 = d^2 \\ \bar{\phi} = q \end{cases} \tag{51}$$

By imposing the discriminant to zero of the corresponding second-order equations:

$$k_{1,2} = \pm\sqrt{\frac{-4c \cdot d^2}{b^2 - 4ac}} \in \mathbb{R}, \quad q_{1,2} = \pm\sqrt{\frac{-4a \cdot d^2}{b^2 - 4ac}} \in \mathbb{R} \tag{52}$$

The outer region, denoted as $\mathrm{R_{outer}} = [k_2, k_1] \times [q_2, q_1]$, circumscribes the ellipse with an associated probability of

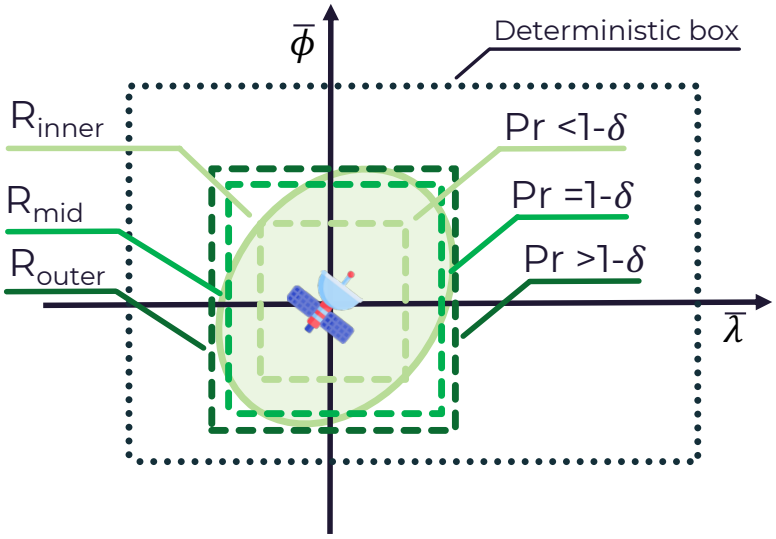

Fig. 5 Overview on the $\mathrm{R_{outer}}$, $\mathrm{R_{mid}}$ and $\mathrm{R_{inner}}$ rectangle domains with associated probabilities.

$1 - \delta$, leading to:

$$\Pr(\boldsymbol{r}_\mathrm{p} \mid (\lambda(\boldsymbol{r}_\mathrm{p}), \phi(\boldsymbol{r}_\mathrm{p})) \in \mathrm{R_{outer}}) > 1 - \delta \tag{53}$$

When it comes to $\mathrm{R_{inner}} = [\hat{k}_2, \hat{k}_1] \times [\hat{q}_2, \hat{q}_1]$, an additional condition on the rectangle aspect ratio is enforced:

$$\beta = \frac{q_1}{k_1}, \quad \hat{q} = \beta k \tag{54}$$

The underlying idea involves identifying an inner rectangle, sharing the identical aspect ratio as $\mathrm{R_{outer}}$. This proves crucial as the subsequent application of the bisection-like algorithm to derive $\mathrm{R_{mid}}$ is uniquely tailored for one-dimensional functions.

$$\begin{cases} a\bar{\lambda}^2 + b\bar{\lambda}\bar{\phi} + c\bar{\phi}^2 = d^2 \\ \bar{\lambda} = k \\ \bar{\phi} = \beta k \end{cases} \tag{55}$$

By substituting $\bar{\lambda}$ and $\bar{\phi}$ in the ellipse equation, it results in:

$$\hat{k}_{1,2} = \pm\sqrt{\frac{d^2}{a + b \cdot \beta + c \cdot \beta^2}} \in \mathbb{R}, \quad \hat{q}_{1,2} = \beta \hat{k}_{1,2} \tag{56}$$

$\mathrm{R}_{\text{inner}}$ will adhere to the following condition:

$$\Pr(\boldsymbol{r}_{\mathrm{p}} \mid (\lambda(\boldsymbol{r}_{\mathrm{p}}), \phi(\boldsymbol{r}_{\mathrm{p}})) \in \mathrm{R}_{\text{inner}}) < 1 - \delta \tag{57}$$

Now, the one-dimensional decision variable $0 \leq \omega \leq 1$ drives the bisection algorithm, shaping the domain between $\mathrm{R}_{\text{inner}}$ and $\mathrm{R}_{\text{outer}}$ with $\mathrm{R}_{\text{int}}(\omega)$:

$$\begin{aligned} \mathrm{R}_{\text{int}}(\omega) =& [\hat{k}_2 + \omega(k_2 - \hat{k}_2), \hat{k}_1 + \omega(k_1 - \hat{k}_1)] \times \\ & [\beta\hat{k}_2 + \omega(q_2 - \beta\hat{k}_2), \beta\hat{k}_1 + \omega(q_1 - \beta\hat{k}_1)] \end{aligned} \tag{58}$$

While Eq. (58) may initially seem intricate, evaluate for $\omega = 0$ and $\omega = 1$. In the former case, $\mathrm{R}_{\text{int}}(0) \equiv \mathrm{R}_{\text{inner}}$, while for $\mathrm{R}_{\text{int}}(1) \equiv \mathrm{R}_{\text{outer}}$. Ultimately, the bisection is configured as follows:

1) Set two initial boundary values for ω; namely, $\omega_1 = 0$ and $\omega_2 = 1$;
2) Evaluate the Gaussian PDF over $\mathrm{R}_{\text{int}}(\omega)$ for ω_1 and ω_2 adopting Sec. II.D as an integration scheme and integration error check from Alg. 2;
3) Iteratively update ω_1 or ω_2, taking as cost functions $J = \Pr(\boldsymbol{r}_{\mathrm{p}} \mid (\lambda(\boldsymbol{r}_{\mathrm{p}}), \phi(\boldsymbol{r}_{\mathrm{p}})) \in \mathrm{R}_{\text{int}}(\omega)) - (1 - \delta)$.
4) Do step $2 - 3$ until $|J| \leq \epsilon$ with ϵ being a prescribed tolerance.

Suppose obtaining the value of ω^* from the preceding bisection method, ensuring that:

$$\Pr(\boldsymbol{r}_{\mathrm{p}} \mid (\lambda(\boldsymbol{r}_{\mathrm{p}}), \phi(\boldsymbol{r}_{\mathrm{p}})) \in \mathrm{R}_{\text{int}}(\omega^*)) \approx 1 - \delta \tag{59}$$

Therefore, $\mathrm{R}_{\text{mid}} \equiv \mathrm{R}_{\text{int}}(\omega^*)$. The chance constraint introduced with Eqs. (36a) and (36b) is now transformed into:

$$\boldsymbol{G}_i^j \boldsymbol{x}_i^j + \boldsymbol{v}_{\text{sk},i}^j \succeq \boldsymbol{\gamma}_0 - \Delta\boldsymbol{\gamma} + \Delta\boldsymbol{\gamma}_{joint,i}^{\text{lo},j} + \boldsymbol{d}_i^j \qquad \text{for } i \in \{1, \ldots, N\} \tag{60a}$$

$$\boldsymbol{G}_i^j \boldsymbol{x}_i^j + \boldsymbol{v}_{\text{sk},i}^j \preceq \boldsymbol{\gamma}_0 + \Delta\boldsymbol{\gamma} - \Delta\boldsymbol{\gamma}_{joint,i}^{\text{up},j} + \boldsymbol{d}_i^j, \qquad \text{for } i \in \{1, \ldots, N\} \tag{60b}$$

with:

$$\Delta\boldsymbol{\gamma}_{joint,i}^{\text{lo},j} = \Delta\boldsymbol{\gamma}_{joint,i}^{\text{up},j} = \begin{bmatrix} \hat{k}_{1,i}^j + \omega_i^{*,j}(k_{1,i}^j - \tilde{k}_{1,i}^j) \\ \beta\hat{k}_{1,i}^j + \omega_i^{*,j}(q_{1,i}^j - \beta\hat{k}_{1,i}^j) \end{bmatrix} \tag{61}$$

Although initially presented in a two-dimensional context, the joint constraint initialization readily applies to higher

dimensions by simply using the probability expression as a function of SMD described in Sec. II.C and by imposing the aspect ratio condition on R_{inner}.

Algorithm 2 2D Gaussian Area Computation Algorithm

$prob_tot$ = area_gaussian(fun, x_lim_1, x_lim_2, y_lim_1, y_lim_2, n, $Gauss_x$, $Gauss_w$, ϵ_p)
  fun: the integrand function
  x_lim_1, x_lim_1: the first integral bound on the x/y axes
  y_lim_1, y_lim_2: the first integral bound on the x/y axes
  n: number of nodes for each dimension
  $Gauss_x$, $Gauss_w$: precomputed nodes and weights for different n.
  ϵ_p minimum percentual error
  Compute the probability p_1 over a rectangular domain given pre-computed nodes and weights:
  p_1 = area_gaussian_2D(fun, x_lim_1, x_lim_2, y_lim_1, y_lim_2, n, $Gauss_x$, $Gauss_w$)
  limiting upper probability p_2
  $p_2 = 1$
while err>ϵ_p **do**
    n = n +1
    p_2 = area_gaussian_2D(fun, x_lim_1, x_lim_2, y_lim_1, y_lim_2)
    $err = \dfrac{|p_2 - p_1|}{p_2}$
    $p_1 = p_2$
end while
  $p_tot = p_2$

1. IRA algorithm for joint constraints in a rectangular-shaped domain

Similarly to the individual chance constraint, one or more nodes may become active during the optimization routine, also caused by linearization errors along the j iterations as in Fig. 6. To address this, a practical solution to relax the

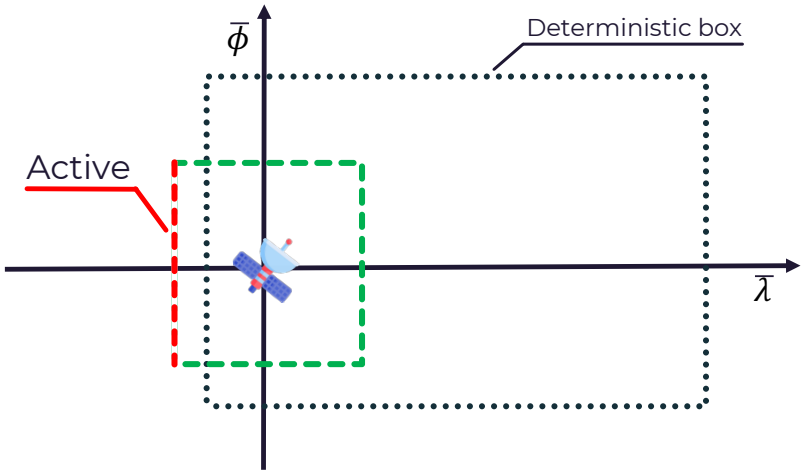

Fig. 6 Representation of an active joint constraint.

tightness of the chance constraint could involve considering an adaptation to the IRA algorithm.

In Eqs. (60a)(60b) during the j-th iteration ($j > 1$) for the i-th node, assume, before invoking the optimization

routine, that there are $0 \leq c_{act} \leq 4$ active constraints and $c_{in} = 1 - c_{act}$ inactive ones. If $c_{act} = 4$ for at least one node, further optimization is impossible, triggering an error. Restrict our analysis to $0 \leq c_{act} \leq 3$ and define the following Boolean vector variables to label active and inactive constraints $\boldsymbol{b}^{\text{lo}}_{\text{act}}$, $\boldsymbol{b}^{\text{up}}_{\text{act}}$, $\boldsymbol{b}^{\text{lo}}_{\text{in}}$, and $\boldsymbol{b}^{\text{lo}}_{\text{in}}$:

$$
\begin{aligned}
b^{\text{lo}}_{\text{act},m} &= \begin{cases} 1, \text{ if Eq. (60a)}_m \text{is active for } m \in [1,2] \\ 0, \text{ otherwise} \end{cases}, b^{\text{lo}}_{\text{in},m} = \neg b^{\text{lo}}_{\text{act},m} \\
b^{\text{up}}_{\text{act},m} &= \begin{cases} 1, \text{ if Eq. (60b)}_m \text{is active for } m \in [1,2] \\ 0, \text{ otherwise} \end{cases}, b^{\text{up}}_{\text{in},m} = \neg b^{\text{up}}_{\text{act},m}
\end{aligned}
\tag{62}
$$

For $m = 1$, it relates to constraints on the longitude λ, and for $m = 2$, it pertains to constraints on the latitude ϕ. The symbol $\neg$ is the one complement operator. To simplify the derivation of the final IRA algorithm, omit the indices i and j, as done in the previous section. The updated IRA algorithm starts out with loosening active constraints:

$$
\begin{aligned}
\Delta\boldsymbol{\gamma}^{\text{lo}}_{\text{joint}}\left(\boldsymbol{b}^{\text{lo}}_{\text{act}}\right) &= \left(1 - \frac{\tau}{c_{\text{act}}}\right)\left(\bar{\boldsymbol{\gamma}}\left(\boldsymbol{b}^{\text{lo}}_{\text{act}}\right) - \boldsymbol{\gamma}_0\left(\boldsymbol{b}^{\text{lo}}_{\text{act}}\right) + \Delta\boldsymbol{\gamma}\left(\boldsymbol{b}^{\text{lo}}_{\text{act}}\right)\right) \\
\Delta\boldsymbol{\gamma}^{\text{up}}_{\text{joint}}\left(\boldsymbol{b}^{\text{up}}_{\text{act}}\right) &= \left(1 - \frac{\tau}{c_{\text{act}}}\right)\left(\boldsymbol{\gamma}_0\left(\boldsymbol{b}^{\text{up}}_{\text{act}}\right) + \Delta\boldsymbol{\gamma}\left(\boldsymbol{b}^{\text{up}}_{\text{act}}\right) - \bar{\boldsymbol{\gamma}}\left(\boldsymbol{b}^{\text{up}}_{\text{act}}\right)\right)
\end{aligned}
\tag{63}
$$

Evaluating Eq. (63) for $\boldsymbol{b}^{\text{lo}}_{\text{act}}$ and $\boldsymbol{b}^{\text{up}}_{\text{act}}$ makes it adaptable to any configuration of active constraints. The parameter τ weighs the proximity of the prior active constraint to the deterministic box outlined by the green dotted rectangle R_{temp} in Fig. 7. Dividing τ by c_{act} heightens stringency for multiple simultaneous active constraints. The following step is to

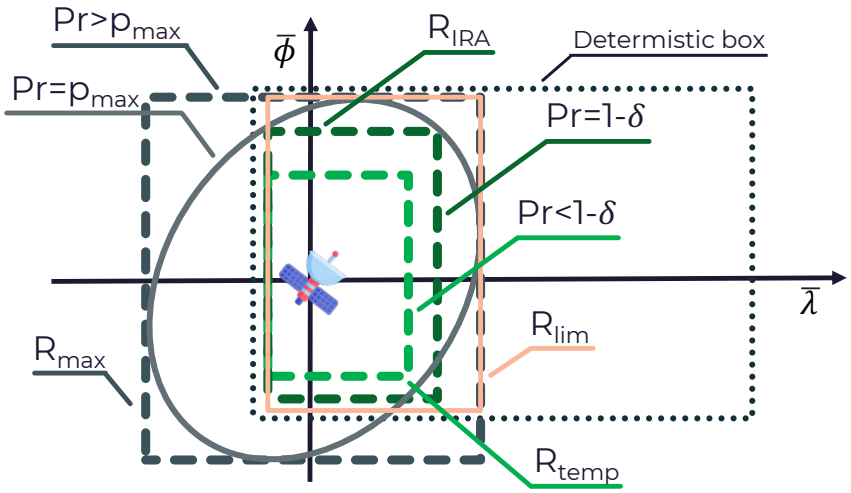

Fig. 7 IRA algorithm for joint chance constraints in rectangular keep-in domains.

extend $\mathrm{R_{temp}}$ to cover an area within the deterministic box while maintaining a violation δ. A procedure akin to the chance constraint initialization determines lower and upper rectangular boundaries, enforcing a prescribed violation with a Gaussian PDF. The lower boundary is already set by $\mathrm{R_{temp}} \in [-\Delta\boldsymbol{\gamma}^{\mathrm{lo}}_{\mathrm{joint},1}, \Delta\boldsymbol{\gamma}^{\mathrm{up}}_{\mathrm{joint},1}] \times [-\Delta\boldsymbol{\gamma}^{\mathrm{lo}}_{\mathrm{joint},2}, \Delta\boldsymbol{\gamma}^{\mathrm{up}}_{\mathrm{joint},2}]$ featuring a probability $\mathrm{Pr} < 1 - \delta$ after relaxing the active constraints. The outer instead takes inspiration from the analytical Gaussian PDF under SMD:

$$d_{\max} = \sqrt{-2\ln(\delta_{\max})}, \quad \delta_{\max} \ll \delta \wedge \delta_{\max} > 0 \tag{64}$$

Using Eq. (52), calculate $k_{\max,1,2}$ and $q_{\max,1,2}$. If $\mathrm{R_{max}}$ has one or more edges extending beyond the deterministic box, depicted by a dark blue rectangle in Fig. 7, the IRA update may be ineffective. To prudently establish a limiting outer rectangle $\mathrm{R_{lim}}$ in pink, one must factor into the deterministic box edges. To this end, build a matrix containing the longitude or latitude distance from the mean $\bar{\boldsymbol{\gamma}}$ for $\mathrm{R_{max}}$ and the deterministic box:

$$\begin{aligned} \boldsymbol{H}^{\mathrm{lo}} =& [\boldsymbol{r}_{\max}, (1-\eta)\,(\bar{\boldsymbol{\gamma}} - \boldsymbol{\gamma}_0 + \Delta\boldsymbol{\gamma})], \quad \boldsymbol{r}_{\max} = [k_{\max,1}, q_{\max,1}]^{\top}, \\ \boldsymbol{H}^{\mathrm{up}} =& [\boldsymbol{r}_{\max}, (1-\eta)\,(\boldsymbol{\gamma}_0 + \Delta\boldsymbol{\gamma} - \bar{\boldsymbol{\gamma}})] \end{aligned} \tag{65}$$

$\eta \ll 1 \wedge \eta > 0$ is a safety measure in case the rectangle with $\mathrm{Pr} = 1 - \delta$ touches the deterministic box. The the minimum vector of distances from the $\bar{\boldsymbol{\gamma}}$ will then be:

$$g^{\mathrm{lo}}_k = \min(\boldsymbol{H}^{\mathrm{lo}}_{k,l}), \;\; g^{\mathrm{up}}_k = \min(\boldsymbol{H}^{\mathrm{up}}_{k,l}), \quad k, l \in [1, 2] \tag{66}$$

The resulting $\mathrm{R_{lim}}$ is constrained within the interval $[-g^{\mathrm{lo}}_1, g^{\mathrm{up}}_1] \times [-g^{\mathrm{lo}}_2, g^{\mathrm{up}}_2]$, visually represented by the pink rectangle in Fig. 7. The previous passage might appear unnecessary, as one could have solely exploited the deterministic box as the limiting outer rectangle. However, adopting such an approach would incur a higher computational cost due to the larger rectangular domain during the bisection routine. Moreover, integrating with numerical methods could lead to a null integral for functions that are nearly zero across the majority of their domains. After having explicitly defined the limiting rectangles as $\mathrm{R_{temp}}$ and $\mathrm{R_{lim}}$, proceed with the bisection method. Consistent with the joint constraint initialization, choose the one-dimensional decision variable ω for algorithm execution to vary the rectangular domain as a function of it from $\mathrm{R_{temp}}$ to $\mathrm{R_{lim}}$:

$$\begin{aligned} \mathrm{R_{IRA}}(\omega) =& \Big[-\left(\Delta\gamma^{\mathrm{lo}}_{\mathrm{joint},1} + \omega b^{\mathrm{lo}}_{\mathrm{in},1}\left(g^{\mathrm{lo}}_1 - \Delta\gamma^{\mathrm{lo}}_{\mathrm{joint},1}\right)\right), \\ & \left(\Delta\boldsymbol{\gamma}^{\mathrm{up}}_{\mathrm{joint},1} + \omega b^{\mathrm{up}}_{\mathrm{in},1}\left(g^{\mathrm{up}}_1 - \Delta\gamma^{\mathrm{up}}_{\mathrm{joint},1}\right)\right)\Big] \times \\ & \Big[-\left(\Delta\gamma^{\mathrm{lo}}_{\mathrm{joint},2} + \omega b^{\mathrm{lo}}_{\mathrm{in},2}\left(g^{\mathrm{lo}}_2 - \Delta\gamma^{\mathrm{lo}}_{\mathrm{joint},2}\right)\right), \\ & \left(\Delta\gamma^{\mathrm{up}}_{\mathrm{joint},2} + \omega b^{\mathrm{up}}_{\mathrm{in},2}\left(g^{\mathrm{up}}_2 - \Delta\gamma^{\mathrm{up}}_{\mathrm{joint},2}\right)\right)\Big] \end{aligned} \tag{67}$$

If the condition:

$$\Pr(\boldsymbol{r}_{\mathrm{p}} \mid (\lambda(\boldsymbol{r}_{\mathrm{p}}), \phi(\boldsymbol{r}_{\mathrm{p}})) \in \mathrm{R}_{\mathrm{lim}}) \geq 1 - \delta \tag{68}$$

holds, then for an optimal ω^* where $0 < \omega^* \leq 1$:

$$\Pr\left(\boldsymbol{r}_{\mathrm{p}} \mid (\lambda(\boldsymbol{r}_{\mathrm{p}}), \phi(\boldsymbol{r}_{\mathrm{p}})) \in \mathrm{R}_{\mathrm{IRA}}(\omega^*)\right) \approx 1 - \delta \tag{69}$$

Otherwise, the optimization problem becomes unfeasible. For simplicity, the updated IRA is illustrated in Fig. 7 for a single node featuring one active constraint. Expanding this approach to simultaneously handle all nodes in a programming environment can be effortlessly accomplished through vectorization techniques.The last step is to update $\Delta\boldsymbol{\gamma}^{\mathrm{lo}}_{joint}$ and $\Delta\boldsymbol{\gamma}^{\mathrm{lo}}_{joint}$ after IRA:

$$\begin{aligned}
\Delta\boldsymbol{\gamma}^{\mathrm{lo}}_{joint}(\boldsymbol{b}^{\mathrm{lo}}_{\mathrm{in}}) &= \Delta\boldsymbol{\gamma}^{\mathrm{lo}}_{\mathrm{joint}}(\boldsymbol{b}^{\mathrm{lo}}_{\mathrm{in}}) + \omega^* \left(\boldsymbol{g}^{\mathrm{lo}}(\boldsymbol{b}^{\mathrm{lo}}_{\mathrm{in}}) - \Delta\boldsymbol{\gamma}^{\mathrm{lo}}_{\mathrm{joint}}(\boldsymbol{b}^{\mathrm{lo}}_{\mathrm{in}})\right) \\
\Delta\boldsymbol{\gamma}^{\mathrm{up}}_{joint}(\boldsymbol{b}^{\mathrm{up}}_{\mathrm{in}}) &= \Delta\boldsymbol{\gamma}^{\mathrm{up}}_{\mathrm{joint}}(\boldsymbol{b}^{\mathrm{up}}_{\mathrm{in}}) + \omega^* \left(\boldsymbol{g}^{\mathrm{up}}(\boldsymbol{b}^{\mathrm{up}}_{\mathrm{in}}) - \Delta\boldsymbol{\gamma}^{\mathrm{up}}_{\mathrm{joint}}(\boldsymbol{b}^{\mathrm{up}}_{\mathrm{in}})\right)
\end{aligned} \tag{70}$$

Evaluating for $\boldsymbol{b}^{\mathrm{lo}}_{\mathrm{in}}$ and $\boldsymbol{b}^{\mathrm{up}}_{\mathrm{in}}$ leaves the relaxed active constraints untouched. Lastly, Eqs. (36a) and (36b) are now transformed into:

$$\boldsymbol{G}^j_i \boldsymbol{x}^j_i + \boldsymbol{v}^j_{\mathrm{sk},i} \succeq \boldsymbol{\gamma}_0 - \Delta\boldsymbol{\gamma} + \Delta\boldsymbol{\gamma}^{\mathrm{lo},j}_{joint,i} + \boldsymbol{d}^j_i \qquad \text{for } i \in \{1,\ \ldots,\ N\} \tag{71a}$$

$$\boldsymbol{G}^j_i \boldsymbol{x}^j_i + \boldsymbol{v}^j_{\mathrm{sk},i} \preceq \boldsymbol{\gamma}_0 + \Delta\boldsymbol{\gamma} - \Delta\boldsymbol{\gamma}^{\mathrm{up},j}_{joint,i} + \boldsymbol{d}^j_i, \qquad \text{for } i \in \{1,\ \ldots,\ N\} \tag{71b}$$

E. Multi Initial Orbit Determinations

Integrating Orbit Determination (OD) into chance-constrained optimization represents a transformative approach to improving the solution search space for longer maneuvers. By periodically mitigating orbital uncertainty, this strategy addresses a key challenge highlighted earlier - the tendency for uncertainty to inflate - impeding stochastic-based optimization techniques as in the left graph of Fig 8.

Consider planning an OD at $t_m \in \{t_0, t_1, \ldots, t_N\}$, where $N + 1$ is the number of nodes. The combined CAM and SK problem run in two separate branches $\boldsymbol{t_1} = \{t_0, \ldots, t_m\}$ and $\boldsymbol{t_2} = \{t_m, \ldots, t_N\}$ with different initial conditions for both the mean state and the covariance. Expressly, for $\boldsymbol{t_1}$, the initial conditions mirror the ones of Eq. (40) except for the final integration time set to t_m. CAM instead in $\boldsymbol{t_2}$ has updated orbital information regarding the mean state and the associated covariance after OD. Commencing with the mean state at t_m:

$$\boldsymbol{x}_{\mathrm{p},m^+} \sim \mathcal{N}(\bar{\boldsymbol{\mu}}^j_{m^-}, \boldsymbol{C}^j_{\mathrm{p},m^-}) \tag{72}$$

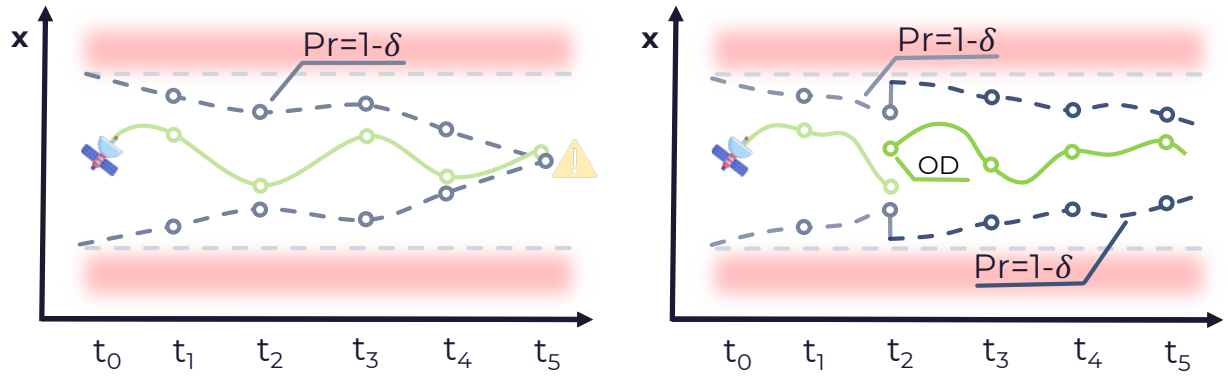

Fig. 8 Uncertainty growth results in a null solution space in (a). OD reduces orbital uncertainty in (b).

$\bar{\boldsymbol{\mu}}^{j}_{m^-,\mathrm{p}}$ is the primary mean state and it stems from the solution of Eq. (40) at t_m; $\boldsymbol{C}^{j}_{\mathrm{p},m^-}$ relates to the primary covariance propagated through the STM. $\bar{\boldsymbol{\mu}}^{0}_{\mathrm{p},m^+}$ is just a realization from the propagated Gaussian uncertainty distribution at t_m. Every branch between two OD processes is treated as an individual trajectory optimization problem. Moving on to $\boldsymbol{C}_{p,m^+}$, it has the same eigenvalues of $\boldsymbol{C}_{\mathrm{p},0}$ (maximum uncertainty over the tangential direction), and it mimics a typical covariance matrix after a synthetic OD process:

$$\boldsymbol{C}_{\mathrm{p},0} = \boldsymbol{P}\boldsymbol{\Lambda}\boldsymbol{P}^{-1} \tag{73}$$

It is then framed from Local Vertical Local Horizontal (LVLH) to ECI by a simple matrix rotation:

$$\boldsymbol{R}_{\mathrm{LVLH}\to\mathrm{ECI,\,TOT},m^+} = \begin{bmatrix} \boldsymbol{R}_{\mathrm{LVLH}\to\mathrm{ECI},m^+} & \boldsymbol{0}_{3\times3} \\ \boldsymbol{0}_{3\times3} & \boldsymbol{R}_{\mathrm{LVLH}\to\mathrm{ECI},m^+} \end{bmatrix}$$
$$\boldsymbol{C}_{\mathrm{p},m^+} = \boldsymbol{R}_{\mathrm{LVLH}\to\mathrm{ECI,\,TOT},m^+}\boldsymbol{\Lambda}(\boldsymbol{R}_{\mathrm{LVLH}\to\mathrm{ECI,\,TOT},m^+})^{\top} \tag{74}$$

With a shrunk covariance, as evident in Fig. 8, the chance constraint boundary instantly drops at the OD time, thereby expanding the window for maneuver planning. The showcased procedure can be easily extended to multiple ODs, leading to several local trajectory optimization branches.

IV. Results

A. Test case

To achieve comprehensive CAM and SK understanding in GEO, long-term encounter modeling involves constructing primary and secondary ballistic orbits that keep two objects close for multiple Earth revolutions, as shown in Fig. 9. The

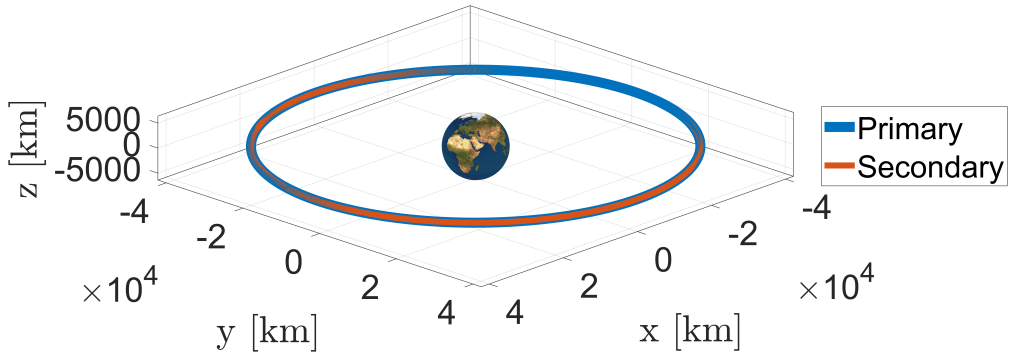

Fig. 9 Primary and secondary orbit representation.

.

states for both objects are depicted at Time of Closest Approach (TCA) ($t = 0$) for in Tabs. 2, 3.

Table 2 Primary position and velocity at TCA ($t = 0$)

State Parameter	x	y	z
Position (km)	9334.756	41120.986	1.571
Velocity (km/s)	-2.9982	0.6808	0.0064

Table 3 Secondary position and velocity at TCA ($t = 0$)

State Parameter	x	y	z
Position (km)	9333.589	41120.363	1.573
Velocity (km/s)	-2.998	0.681	0.006

Regarding the primary and secondary initial state uncertainty, they are expressed via the covariance matrices $\boldsymbol{C}_{\mathrm{p},0}$ and $\boldsymbol{C}_{\mathrm{s},0}$ with units of measure $\left[\mathrm{km}^2\right]$, $\left[\frac{\mathrm{km}^2}{\mathrm{s}}\right]$ and $\left[\frac{\mathrm{km}^2}{\mathrm{s}^2}\right]$ in the ECI r.f.:

$$\boldsymbol{C}_{\mathrm{p},0} = \left[\boldsymbol{C}_{p,0_1}\ \boldsymbol{C}_{p,0_2}\right],\ \ \boldsymbol{C}_{\mathrm{s},0} = \left[\boldsymbol{C}_{s,0_1}\ \boldsymbol{C}_{s,0_2}\right] \tag{75}$$

where $\boldsymbol{C}_{p,0_1}, \boldsymbol{C}_{p,0_2}, \boldsymbol{C}_{s,0_1}\ \boldsymbol{C}_{s,0_2}$ are found in Eqs. (76)(77)(78)(79).

$$C_{p,0_1} = \begin{bmatrix} 5.47 \times 10^{-6} & 6.75 \times 10^{-7} & -1.60 \times 10^{-9} \\ 6.75 \times 10^{-7} & 2.65 \times 10^{-6} & -5.41 \times 10^{-9} \\ -1.60 \times 10^{-9} & -5.41 \times 10^{-9} & 5.63 \times 10^{-8} \\ & \mathbf{0}_{3\times3} & \end{bmatrix} \tag{76}$$

$$C_{p,0_2} = \begin{bmatrix} & \mathbf{0}_{3\times3} & \\ 1.34 \times 10^{-8} & 2.70 \times 10^{-9} & -6.08 \times 10^{-12} \\ 2.70 \times 10^{-9} & 2.18 \times 10^{-9} & -3.45 \times 10^{-12} \\ -6.08 \times 10^{-12} & -3.45 \times 10^{-12} & 5.63 \times 10^{-10} \end{bmatrix} \tag{77}$$

$$C_{s,0_1} = \begin{bmatrix} 2.87 \times 10^{-5} & -1.62 \times 10^{-5} & 3.33 \times 10^{-8} \\ -1.62 \times 10^{-5} & 9.63 \times 10^{-5} & -1.57 \times 10^{-7} \\ 3.33 \times 10^{-8} & -1.57 \times 10^{-7} & 2.03 \times 10^{-5} \\ & \mathbf{0}_{3\times3} & \end{bmatrix} \tag{78}$$

$$C_{s,0_2} = \begin{bmatrix} & \mathbf{0}_{3\times3} & \\ 5.38 \times 10^{-7} & 1.08 \times 10^{-7} & -2.43 \times 10^{-10} \\ 1.08 \times 10^{-7} & 8.70 \times 10^{-8} & -1.38 \times 10^{-10} \\ -2.43 \times 10^{-10} & -1.38 \times 10^{-10} & 2.25 \times 10^{-8} \end{bmatrix} \tag{79}$$

The maneuver timeframe spans from -0.2 to 0.6 orbits of the primary. Specifically, the solution process begins at -0.2 orbits where both objects are backwardly propagated from the nominal TCA ($t = 0$) before starting the optimization routine. The SOCP is solved using MOSEK 10.0.24 [47]. Dynamics-wise, the problem relies on the AIDA numerical propagator [45], incorporating essential orbital high-order gravitational harmonics up to the 10-th order, SRP and lunisolar perturbations. The primary, secondary, and simulation parameters are reported in Tabs. 4,5, and 6. Referring to Table 6, n_{orbit} is selected to balance solution optimality, considering firing time selection, constraint satisfaction accuracy (minimizing violations between nodes), and computational efficiency. A finer time grid improves the first two aspects, while a coarser one enhances the latter, requiring a compromise.

Table 4 Primary Spacecraft Properties

Property	Value	Unit
Mass	500	kg
SRP Surface Area (A_{srp})	1	m^2
SRP Coefficient (C_r)	1.31	[-]

Table 5 Secondary Spacecraft Properties

Property	Value	Unit
Mass	50	kg
SRP Surface Area (A_{srp})	0.05	m^2
SRP Coefficient (C_r)	1.31	[-]

B. Individual chance constraint formulation for the station-keeping problem

For starters, the progression of longitude and latitude is depicted in Fig. 10 when integrating SK and CAM without the chance constraint formulation. The blue line corresponds to the ballistic trajectory of the primary, while the orange line links the controlled motion that simultaneously adheres to both constraints. Since the problem is stated as a deterministic SK, the constraints on longitude and latitude, depicted in black (No CC) in Fig. 10, remain unchanged over time.

Table 6 Simulation parameters

Parameter	Value	Unit
Simulation time t	$[-0.2, 0.6]$	primary's orbit
Number of integration nodes per orbit (n_{orbit})	140	[-]
Maximum n. of major iter j	10	[-]
Maximum n. of minor iter i	10	[-]
Control weight c_{cntrl}	7.144^{-6}	[-]
$\tau_{\text{min}}, \tau_{\text{maj}}$	10^{-6}	[-]
Latitude bound ($\Delta\gamma_1$)	0.05	deg
Longitude bound ($\Delta\gamma_2$)	0.05	deg
Maximum acceleration level (u_{max})	$7 \cdot 10^{-5}$	$\frac{\text{m}}{\text{s}^2}$
Limiting IPoC (P_{IC})	10^{-6}	[-]
Overall violation probability (Δ)	0.09	[-]
Initial violation probability per constraint $\left(\delta = \frac{\Delta}{4}\right)$	0.0225	[-]
Weighting parameter for Eq. (63) (τ)	$5 \cdot 10^{-3}$	[-]
Limiting probability for R_{max} (δ_{max})	10^{-3}	[-]
Weighting parameter for Eq. (65) (η)	10^{-3}	[-]

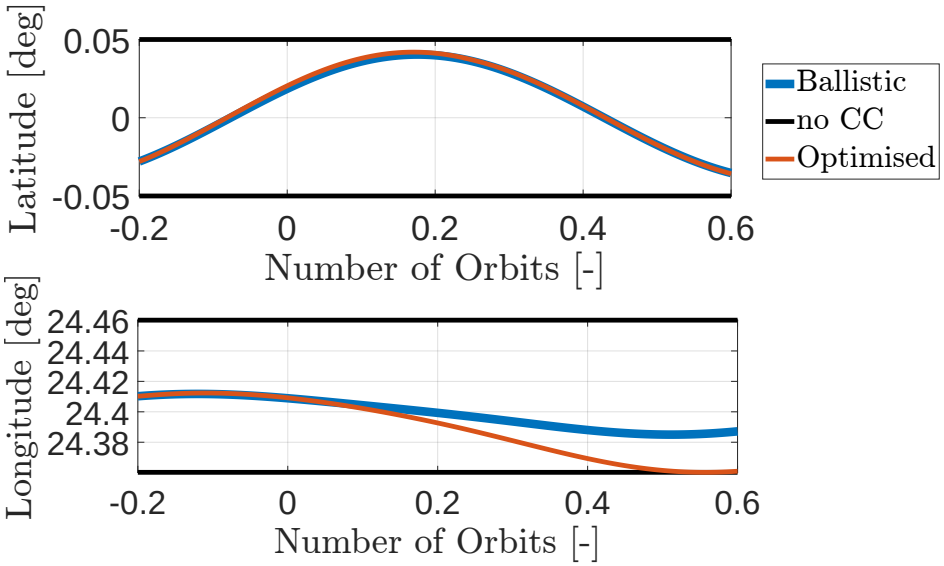

Fig. 10 Latitude and longitude evolution for ballistic motion and deterministic CAM with SK

By introducing the individual chance constraint in Fig. 11, the upper (in red) and lower (in green) boundaries shrink as the uncertainty grows. The longitude is particularly susceptible to this effect, as the tangential direction aligns with the predominant axis of uncertainty. The optimizer additionally counts on the IRA algorithm to address an active constraint about the longitude of the final nodes. The red line ascends, and the green one goes slightly upward, effectively resolving the CCSK problem.

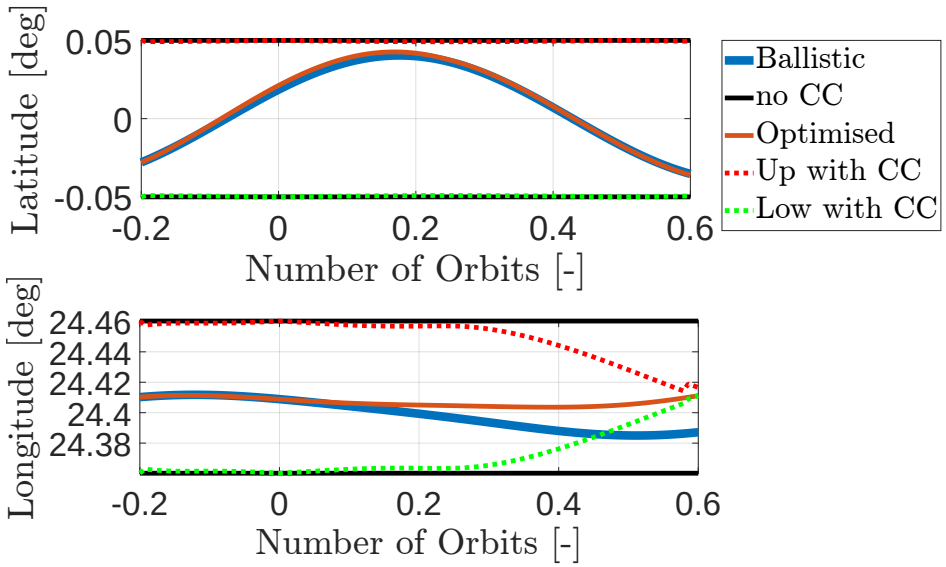

Fig. 11 Latitude and longitude evolution for ballistic motion CAM with individual CCSK.

Another way of spotting when the IRA algorithm comes into play is by looking at the violation probability δ against the simulation time in Fig. 12. As the reader can notice, the red and green colors are connected to the upper and lower boundaries while the black line alludes to the initialization value latitude and longitude wise. If δ stays constant, i.e., equal to the reference setting in black, no violation occurs. Conversely, the last nodes experience three inactive constraints (the lower latitude/longitude and upper latitude) that progressively tighten while the upper longitude constraint loosens.

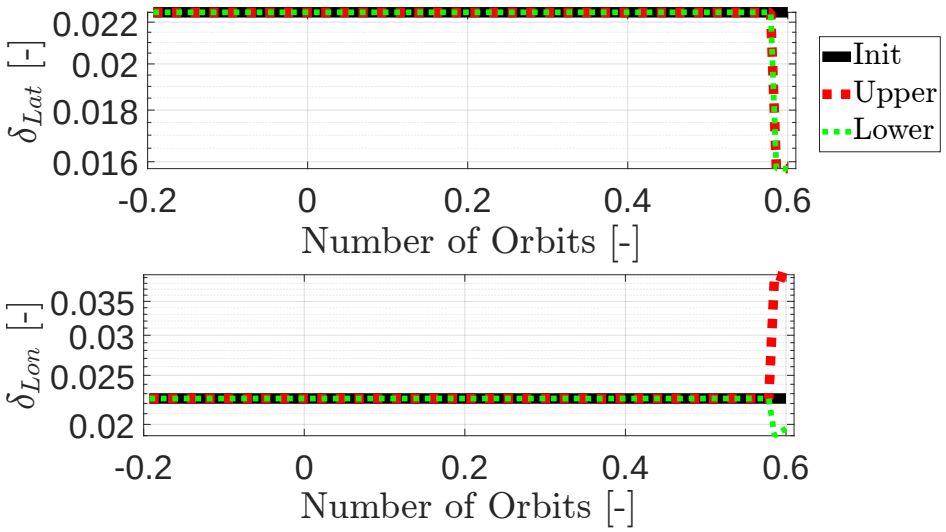

Fig. 12 Violation probability evolution for CAM and individual CCSK.

In addition to SK, the maneuver is considered successful when $P_{IC} \leq 10^{-6}$ for the non-stochastic slot allocation, as shown in Fig. 13. In particular, the blue line, representing IPoC of the ballistic motion, intersects the IPoC threshold

twice. CAM, depicted in orange, effectively maintains a safe separation between the primary and secondary throughout the entire time frame without exceeding the specified limit. The same index is checked for CAM and the individual CCSK in Fig. 14.

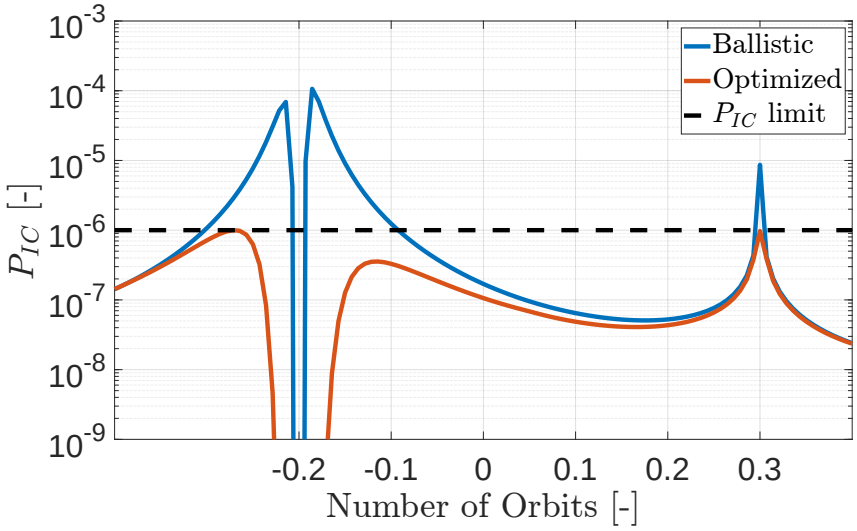

Fig. 13 IPoC evolution for the ballistic motion and the non-stochastic CAM and SK.

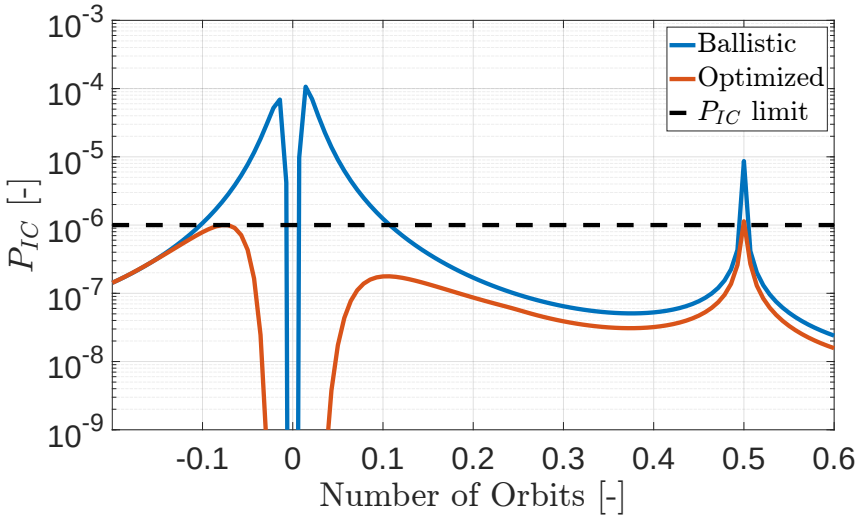

Fig. 14 IPoC evolution for the ballistic motion and CAM with individual CCSK.

Following, Fig. 15 showcases the control profile for the standard CAM and SK. $\tilde{u} = \dfrac{u}{u_{\max}}$ is the non-dimensional acceleration normalized relative the maximum available acceleration $u_{\max}$. Two impulses are ignited, one at the initial time and the other at roughly 0.25 primary revolutions. $\tilde{u}$ in black, and its Radial Transversal Normal (RTN) components in blue, orange, and yellow are persistently confined between 1 and -1, saturating the control and leading to a bang-bang-like profile compatible with low-thrust technology.

The same parameter is analyzed for the stochastic counterpart in Fig. 16. Despite being the norm $\tilde{u}$ close to the one

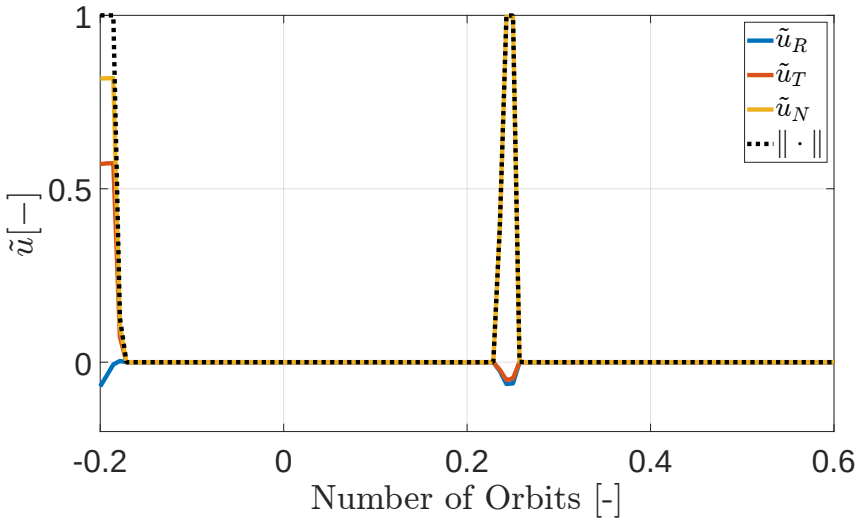

Fig. 15 RTN Acceleration profile for the deterministic CAM and SK.

in Fig. 15, the components are rearranged to conform to the chance constraint formulation.

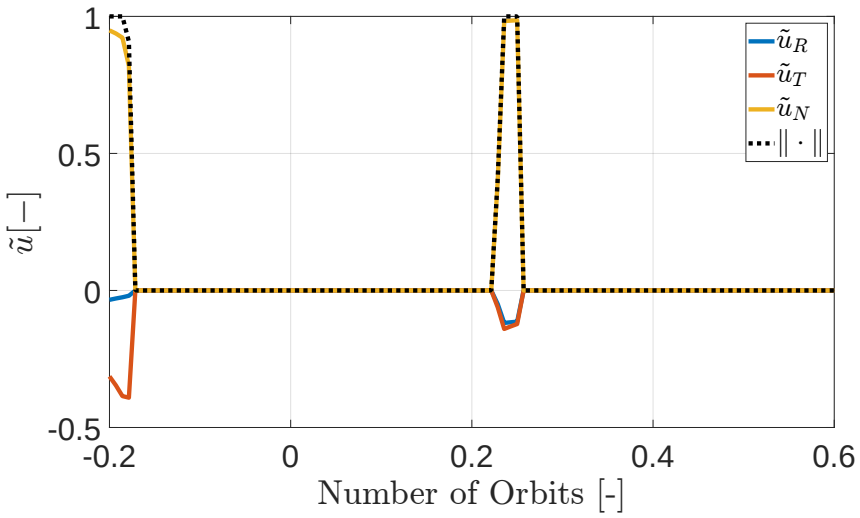

Fig. 16 RTN Acceleration profile for CAM and the individual CCSK.

.

C. Joint Station Keeping Chance Constraint

Taking a closer look at the CAM and joint CCSK, the first quantity of interest is the shape of the boundaries latitude and longitude wise in Fig. 17. The simulation parameters introduced in Sec. III.D, are declared in Table 6.

Unlike the individual chance constraint, the joint one does not uniformly distribute the violation δ across all constraints at initialization, potentially leading to an overestimation of the new boundaries. Furthermore, when the correlation among independent variables approaches 1, treating them as separate entities is statistically unsound. The correlation index is almost null on all the nodes as in Fig. 18.

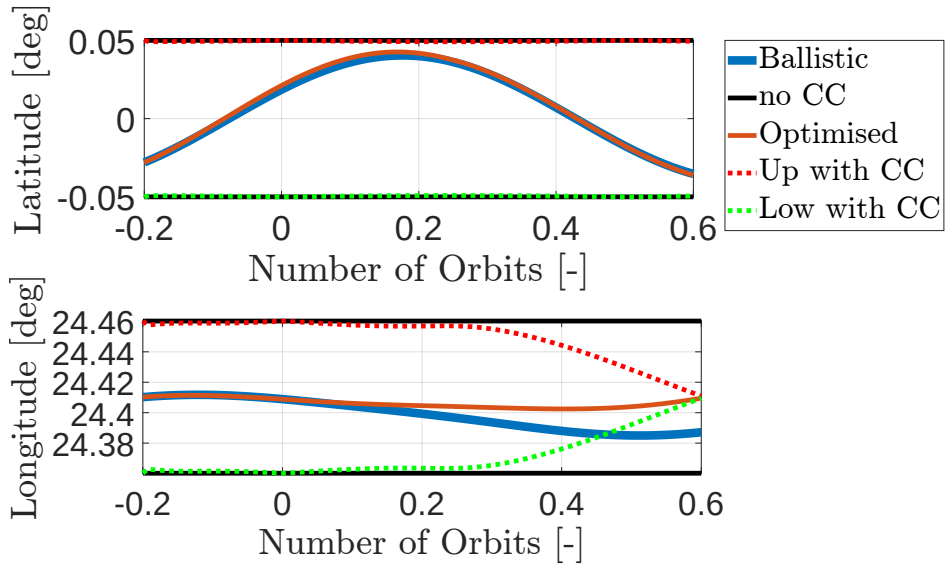

Fig. 17 Latitude and longitude evolution for ballistic motion and CAM with joint CCSK.

In other applications, like dealing with a rectangular domain in ECI coordinates, considering correlations provides a better description of the problem. A noticeable difference between Fig. 17 and Fig. 11 is observed at the final nodes, where the joint formulation a different reshaping of the boundaries when a violation occurs.

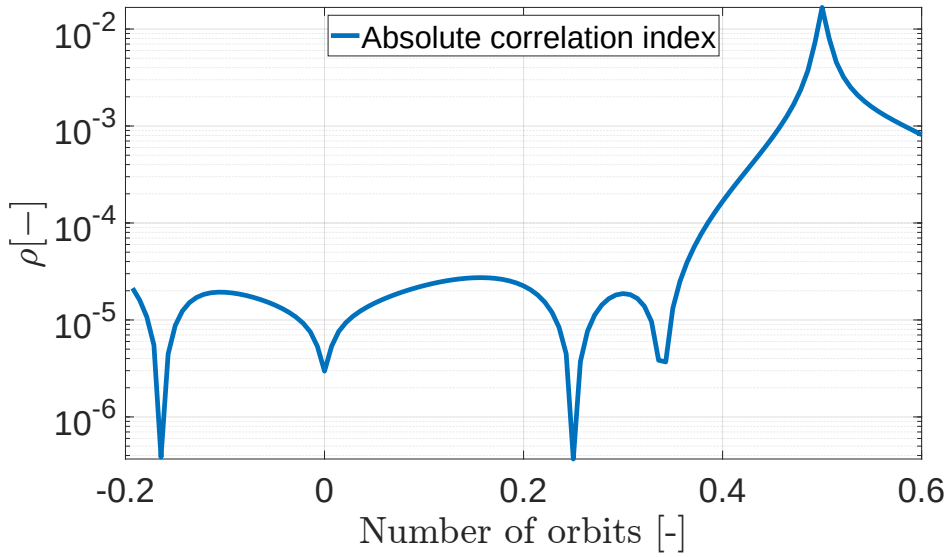

Fig. 18 Correlation index in longitude and latitude coordinates vs maneuvering time.

Moreover, Fig. 19 provides the IPoC trend for the ballistic and optimized maneuver. The joint approach still satisfies the imposed IPoC boundary condition throughout the simulation time window.

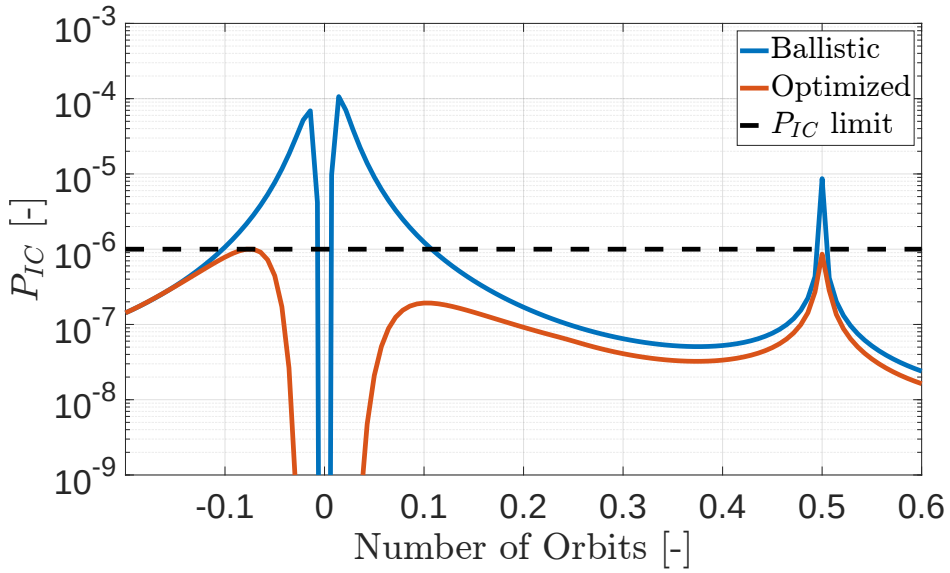

Fig. 19 IPoC evolution for the ballistic motion and CAM with joint CCSK.

D. Perfomance comparison between the CAM and SK strategies

The three methods for embedded CAM and SK are compared in Tables 78. All approaches are accurately represented by the linearization procedure when compared to the nonlinear dynamics propagation, with a maximum position offset of 4.6 m and $2.7 \cdot 10^{-4}$ [m/s] in the worst-case scenario. As expected, the cost function J in the simple CAM and SK results in a lower figure of merit, as the solution space is larger than that of the stochastic SK. Similar considerations apply to Δv; introducing more stringent constraints leads to a slightly higher fuel expenditure. It is worth noting that the number of minor iterations in Table 8 is the sum across all the major iterations.

From a computational perspective, execution times range from 11 to 14.6 seconds. Performance depends on the number of minor i iterations and major j linearizations required for convergence, the number of nodes, and the continuous exchange of information between MATLAB (the user interface) and C++ (the backend) during numerical propagation. The code was run on an Intel(R) Core(TM) i7-10700 CPU @ 2.90GHz with 16 GB of RAM. Reframing this software tool entirely in C++ would likely improve performance and make it more suitable for autonomous and onboard CAM planning.

Table 7 CAM and SK main performance parameters part 1

Case	Max pos. err [m]	Max vel. err [m/s]	J [-]	Total Δv [m/s]
CAM and SK	0.337	$2.696 \cdot 10^{-5}$	$3.7468 \cdot 10^{-5}$	0.238
CAM and individual CCSK	3.2342	$5.2277 \cdot 10^{-5}$	$5.227 \cdot 10^{-5}$	0.315
CAM and Joint CCSK	4.626	$2.688 \cdot 10^{-4}$	$5.172 \cdot 10^{-5}$	0.312

Table 8 CAM and SK main performance parameters part 2

Case	n. of major iter	n. of minor iter	Comp. time [s]
CAM and SK	3	22	11.03
CAM and individual CCSK	3	23	13.32
CAM and Joint CCSK	3	23	14.61

E. Multi Initial Orbit Determinations

In conclusion, the impacts of an OD routine for both objects are evaluated for the joint CAM and CCSK. The trajectory is segmented into three phases: from the initial simulation time until the first OD of the secondary object at approximately 0.2 of the primary's orbit, from 0.2 to the primary orbital update at 0.45 of the primary's orbit, and finally, up to the conclusion of the simulation. In Fig. 20, the ballistic trajectory in blue undergoes a discontinuity at the secondary OD point. It occurs due to a new optimization branch, where the initial primary condition aligns with the optimized trajectory of the previous section. At 0.45, the primary's orbital information is updated, causing a sudden drop in the boundaries owing to reduced uncertainty. The mean state is then sampled from the propagated Gaussian uncertainty computed at the OD time. Please note that the renewed mean state deviates more in terms of longitude from the precedent branch, as the maximum direction of uncertainty consistently aligns with the tangential direction. Frequent ground or space-based observations of the two RSOs have the potential to minimize maneuver costs for the CCSK, thereby ensuring a more optimal solution to the problem.

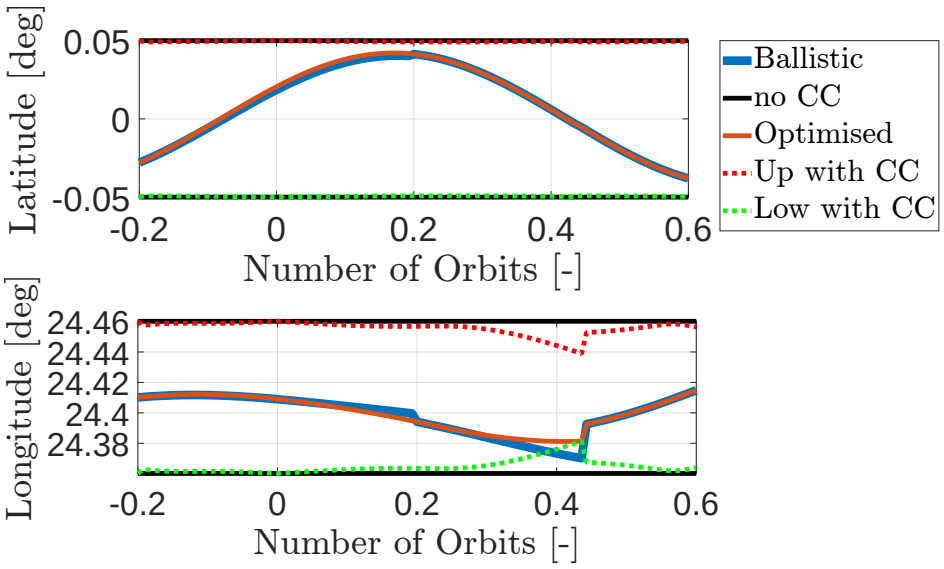

Fig. 20 Latitude and longitude evolution for ballistic motion and OD CAM with CCSK.

In tandem with this, IPoC could benefit from an OD as evident in Fig. 21. After having renewed the secondary mean state and covariance, CAM is no longer obligated to mitigate the risk of a close encounter.

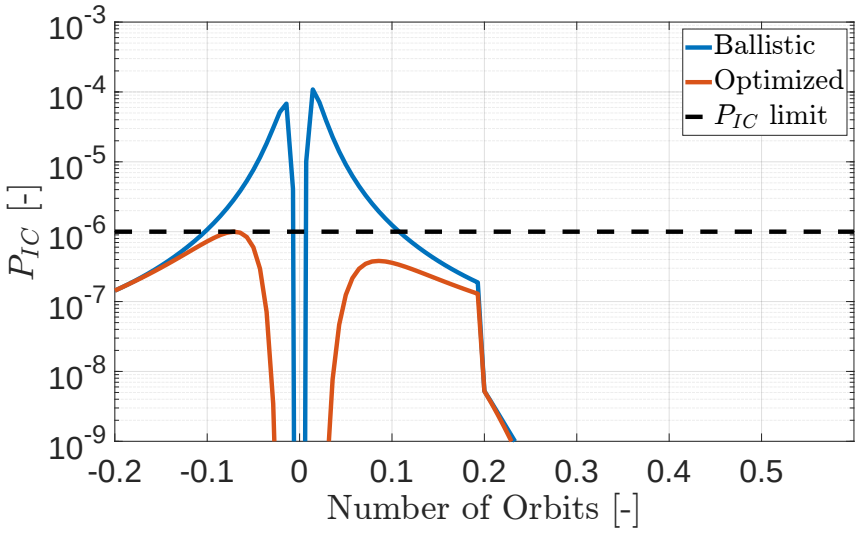

Fig. 21 IPoC evolution for the ballistic motion and OD CAM with CCSK.

V. Conclusions

This paper explores the mathematical derivation of integrated Collision Avoidance Maneuver (CAM) and Chance Constrained Station-Keeping (CCSK) in terms of longitude and latitude. It begins by establishing the optimization problem setup, followed by a linearization process coupled with a convex optimization framework. Two CCSK methods for a rectangular keep-in domain are devised. The individual chance constraint may fall short in depicting the satellite probabilistic distribution in the case of correlated variables. In the presented results, this issue is not exacerbated, as the correlation index is approximately zero. A bespoke joint chance constraint addresses this criticality when handling rectangular keep-in domains like the Station Keeping (SK) one. Ultimately, orbital updates are introduced to mitigate the relentless uncertainty inflation that can impede stochastic trajectory optimization over longer simulation windows. The results, with a dedicated long-term conjunction, highlight key performance parameters. These encompass the evolution in longitude and latitude terms with and without time-dependent SK boundaries, control profiles, and the effectiveness of CAM in ensuring a secure Instantaneous Probability of Collision (IPoC).

References

[1] Montaruli, M. F., Purpura, G., Cipollone, R., De Vittori, A., Facchini, L., Di Lizia, P., Massari, M., Peroni, M., Panico, A., Cecchini, A., and Rigamonti, M., "An orbit determination software suite for Space Surveillance and Tracking applications," *CEAS Space Journal*, Vol. 16, 2024. https://doi.org/10.1007/s12567-024-00535-1.

[2] Office, E. S. D., "ESA'S ANNUAL SPACE ENVIRONMENT REPORT," https://www.sdo.esoc.esa.int/environment_report/Space_Environment_Report_latest.pdf, 2023. Accessed on 09/18/2023.

[3] Dauphin, H., and Boquet, F., "Autonomous Orbit Determination and Station Keeping Control for Competitive Telecom Missions," Final report, European Space Agency, Noordwijk, 2017.

[4] Coppola, V. T., "Including velocity uncertainty in the probability of collision between space objects," *AIAA/AAS Astrodynamics Specialist Conference*, Vol. 143, San Diego, California, 2012, pp. 2159–2178.

[5] Browns, A. C., "Human Spaceflight Recent Conjunctions of Interest Human Spaceflight Screening and Notification," *Proceedings of the USSTRATCOM Conjunction Summary Message Workshop*, 2010, p. 3.

[6] Chan, K., "COMPARISON OF METHODS FOR SPACECRAFT COLLISION PROBABILITY COMPUTATIONS," *International Space Conference of Pacific-basin Societies (ISCOPS), Montreal, Canada*, 2020.

[7] Patera, R., "Satellite Collision Probability for Non-Linear Relative Motion," *AIAA/AAS Astrodynamics Specialist Conference and Exhibit*, Vol. 26, American Institute of Aeronautics and Astronautics, Reston, Virginia, 2002. https://doi.org/10.2514/6.2002-4632.

[8] Alfano, S., "Addressing Nonlinear Relative Motion For Spacecraft Collision Probability," *AIAA/AAS Astrodynamics Specialist Conference and Exhibit*, American Institute of Aeronautics and Astronautics, Reston, Virginia, 2006, pp. 1–10. https://doi.org/10.2514/6.2006-6760.

[9] Alfano, S., "Eliminating Assumptions Regarding Satellite Conjunction Analysis," *The Journal of the Astronautical Sciences*, Vol. 59, 2014, pp. 676–705. https://doi.org/10.1007/s40295-014-0002-4.

[10] Xu, X.-l., and Xiong, Y.-q., "A Research on the Collision Probability Calculation of Space Debris for Nonlinear Relative Motions," *Chinese Astronomy and Astrophysics*, Vol. 35, No. 3, 2011, pp. 304–317. https://doi.org/10.1016/j.chinastron.2011.07.008.

[11] Wen, C., and Qiao, D., "Calculating collision probability for long-term satellite encounters through the reachable domain method," *Astrodynamics*, Vol. 6, No. 2, 2022, pp. 141–159. https://doi.org/10.1007/s42064-021-0119-8.

[12] Jones, B. A., and Doostan, A., "Satellite collision probability estimation using polynomial chaos expansions," *Advances in Space Research*, Vol. 52, No. 11, 2013, pp. 1860–1875. https://doi.org/10.1016/j.asr.2013.08.027, URL http://dx.doi.org/10.1016/j.asr.2013.08.027.

[13] Adurthi, N., and Singla, P., "Conjugate unscented transformation-based approach for accurate conjunction analysis," *Journal of Guidance, Control, and Dynamics*, Vol. 38, No. 9, 2015, pp. 1642–1658. https://doi.org/10.2514/1.G001027.

[14] Zhang, S., Fu, T., Chen, D., and Cao, H., "Satellite instantaneous collision probability computation using equivalent volume cuboids," *Journal of Guidance, Control, and Dynamics*, Vol. 43, No. 9, 2020, pp. 1757–1763. https://doi.org/10.2514/1.G004711.

[15] Pavanello, Z., Pirovano, L., and Armellin, R., "Long-Term Fuel-Optimal Collision Avoidance Maneuvers with Station-Keeping Constraints," *Journal of Guidance, Control, and Dynamics*, 2024, pp. 1–17. https://doi.org/10.2514/1.G007839, URL https://arc.aiaa.org/doi/abs/10.2514/1.G007839https://arc.aiaa.org/doi/10.2514/1.G007839.

[16] Núñez Garzón, U. E., and Lightsey, E. G., "Relating Collision Probability and Separation Indicators in Spacecraft Formation Collision Risk Analysis," *Journal of Guidance, Control, and Dynamics*, Vol. 45, No. 3, 2022, pp. 517–532. https://doi.org/10.2514/1.G0057.

[17] Mueller, J., "Onboard Planning of Collision Avoidance Maneuvers Using Robust Optimization," *AIAA Infotech@Aerospace Conference*, American Institute of Aeronautics and Astronautics, Reston, Virginia, 2009. https://doi.org/10.2514/6.2009-2051, URL https://arc.aiaa.org/doi/10.2514/6.2009-2051.

[18] Serra, R., Arzelier, D., Joldes, M., and Rondepierre, A., "Probabilistic Collision Avoidance for Long-term Space Encounters via Risk Selection," *Advances in Aerospace Guidance, Navigation and Control*, Springer International Publishing, 2015, pp. 679–698. https://doi.org/10.1007/978-3-319-17518-8_39.

[19] Pavanello, Z., Pirovano, L., and Armellin, R., "Long-Term Encounters Collision Avoidance Maneuver Optimization with a Convex Formulation," *33rd AAS/AIAA Space Flight Mechanics Meeting, Austin, Texas, January 15-19 2023*, 2023, pp. 102–110. https://doi.org/10.13140/RG.2.2.10801.35684.

[20] Malyuta, D., Reynolds, T. P., Szmuk, M., Lew, T., Bonalli, R., Pavone, M., and Açıkmeşe, B., "Convex Optimization for Trajectory Generation: A Tutorial on Generating Dynamically Feasible Trajectories Reliably and Efficiently," *IEEE Control Systems*, Vol. 42, No. 5, 2022, pp. 40–113. https://doi.org/10.1109/MCS.2022.3187542, URL https://ieeexplore.ieee.org/document/9905530/.

[21] Losacco, M., Fossà, A., and Armellin, R., "Low-Order Automatic Domain Splitting Approach for Nonlinear Uncertainty Mapping," *Journal of Guidance, Control, and Dynamics*, 2024, pp. 1–20. https://doi.org/10.2514/1.G007271.

[22] Bernardini, N., Baresi, N., and Armellin, R., "State-dependent trust region for successive convex programming for autonomous spacecraft," *Astrodynamics*, 2024, pp. 1–20. https://doi.org/10.1007/s42064-024-0200-1, URL https://link.springer.com/10.1007/s42064-024-0200-1.

[23] Malyuta, D., Yu, Y., Elango, P., and Acikmese, B., "Advances in Trajectory Optimization for Space Vehicle Control," *ArXiv*, 2021. URL {https://arxiv.org/abs/2108.02335},, arXiv:2018.

[24] Wang, Z., "A survey on convex optimization for guidance and control of vehicular systems," *Annual Reviews in Control*, Vol. 57, No. April, 2024, p. 100957.

[25] Armellin, R., "Collision avoidance maneuver optimization with a multiple-impulse convex formulation," *Acta Astronautica*, Vol. 186, 2021, pp. 347–362. https://doi.org/https://doi.org/10.1016/j.actaastro.2021.05.046, URL https://www.sciencedirect.com/science/article/pii/S0094576521002836.

[26] Pavanello, Z., Pirovano, L., Armellin, R., De Vittori, A., and Di Lizia, P., "A Convex Formulation for Collision Avoidance Maneuver Strategies During Low-Thrust Phases," *2024 AIAA SciTech Forum*, 2024. https://doi.org/10.2514/6.2024-0844.

[27] Pavanello, Z., Pirovano, L., Armellin, R., De Vittori, A., and Di Lizia, P., "A Convex Optimization Method for Multiple Encounters Collision Avoidance Maneuvers," *2024 AIAA SciTech Forum*, 2024. https://doi.org/10.2514/6.2024-0845.

[28] Dutta, S., and Misra, A., "Convex optimization of collision avoidance maneuvers in the presence of uncertainty," *Acta Astronautica*, Vol. 197, 2022, pp. 257–268. https://doi.org/10.1016/j.actaastro.2022.05.038.

[29] Zhao, Z., Shang, H., and Wei, B., "Tackling Nonconvex Collision Avoidance Constraints for Optimal Trajectory Planning Using Saturation Functions," *Journal of Guidance, Control, and Dynamics*, Vol. 45, No. 6, 2022, pp. 1002–1016. https://doi.org/10.2514/1.G005052.

[30] Zhao, Z., and Shang, H., "Trajectory Planning for Spacecraft Formation Reconfiguration Using Saturation Function and Difference-of-Convex Decomposition," *IEEE Transactions on Aerospace and Electronic Systems*, Vol. 60, No. 1, 2024, pp. 857–866. https://doi.org/10.1109/TAES.2023.3329476.

[31] Açıkmeşe, B., and Ploen, S. R., "Convex programming approach to powered descent guidance for Mars landing," *Journal of Guidance, Control, and Dynamics*, Vol. 30, No. 5, 2007, pp. 1353–1366. https://doi.org/10.2514/1.27553.

[32] Sagliano, M., "Pseudospectral Convex Optimization for Powered Descent and Landing," *Journal of Guidance, Control, and Dynamics*, Vol. 41, No. 2, 2018, pp. 320–334. https://doi.org/10.2514/1.G002818.

[33] Chai, R., Savvaris, A., Tsourdos, A., and Chai, S., *Stochastic Trajectory Optimization Problems with Chance Constraints*, Springer Singapore, Singapore, 2020, pp. 163–191. https://doi.org/10.1007/978-981-13-9845-2_8, URL https://doi.org/10.1007/978-981-13-9845-2_8.

[34] Chai, R., Chen, K., Cui, L., Chai, S., Inalhan, G., and Tsourdos, A., *Fast Trajectory Optimization with Chance Constraints*, Springer Nature Singapore, Singapore, 2023, pp. 107–130. https://doi.org/10.1007/978-981-99-4311-1_4, URL https://doi.org/10.1007/978-981-99-4311-1_4.

[35] Benedikter, B., Zavoli, A., Wang, Z., Pizzurro, S., and Cavallini, E., "Convex Approach to Covariance Control with Application to Stochastic Low-Thrust Trajectory Optimization," *Journal of Guidance, Control, and Dynamics*, Vol. 45, No. 11, 2022, pp. 2061–2075. https://doi.org/10.2514/1.G006806, URL https://doi.org/10.2514/1.G006806.

[36] Knaup, J. W., and Tsiotras, P., "Computationally Efficient Covariance Steering for Systems Subject to Parametric Disturbances and Chance Constraints," *2023 62nd IEEE Conference on Decision and Control (CDC)*, 2023, pp. 1796–1801. https://doi.org/10.1109/CDC49753.2023.10383671.

[37] Boone, S., and McMahon, J., "Non-Gaussian Chance-Constrained Trajectory Control Using Gaussian Mixtures and Risk Allocation," *2022 IEEE 61st Conference on Decision and Control (CDC)*, 2022, pp. 3592–3597. https://doi.org/10.1109/CDC51059.2022.9993274.

[38] Boone, S., and Mcmahon, J., "Spacecraft maneuver design with non-Gaussian chance constraints using Gaussian mixtures," *61st IEEE Conference on Decision and Control, Cancun, Mexico*, 2022.

[39] Boone, S., and McMahon, J., "Semi-Analytic Spacecraft Maneuver Design with Stochastic Constraints," *2022 American Control Conference (ACC)*, 2022, pp. 1608–1613. https://doi.org/10.23919/ACC53348.2022.9867632.

[40] Van Hessem, D. H., "Stochastic inequality constrained closed-loop model predictive control with application to chemical process operation," doctoral thesis, Mechanical Maritime and Materials Engineering, Delft University of Technology, June 3 2004. To reference this document use: http://resolver.tudelft.nl/uuid:d51025a4-f349-45b8-9121-6bd67aad1297.

[41] Ono, M., and Williams, B. C., "Iterative Risk Allocation: A new approach to robust Model Predictive Control with a joint chance constraint," *2008 47th IEEE Conference on Decision and Control*, 2008, pp. 3427–3432. https://doi.org/10.1109/CDC.2008.4739221.

[42] Bensimhoun, M., "N-dimensional Cumulative Function, and Other Useful Facts about Gaussians and Normal Densities," Tech. rep., Tech. Rep, Jerusalem, Israel, 2009.

[43] Dash, P., *Mixed Quadrature rules for Numerical Integration of functions*, LAP LAMBERT Academic Publishing, 2017. Paperback.

[44] Mathias, R., "Computation of nodes and weights of Gaussian Quadrature rule by using Jacobi method," Masters by research (m.phil.), School of Mathematics, Colleges (2008 onwards) > College of Engineering & Physical Sciences, University of Birmingham, 2010. URL http://etheses.bham.ac.uk/id/eprint/1352, supervisor(s): Roy Mathias.

[45] Morselli, A., Armellin, R., Di Lizia, P., and Bernelli-Zazzera, F., "A high order method for orbital conjunctions analysis: Sensitivity to initial uncertainties," *Advances in Space Research*, Vol. 53, 2013. https://doi.org/10.1016/j.asr.2013.11.038.

[46] NASA's Navigation and Ancillary Information Facility (NAIF), "SPICE: An Observation Geometry System for Space Science Missions," , 2023. URL https://naif.jpl.nasa.gov/naif/index.html.

[47] "MOSEK Documentation," https://www.mosek.com/documentation/, 2023. Accessed on 02/18/2024.